Discrete simulations of a triaxial compression test for sand by DEM

Jan Kozicki[1], Jacek Tejchman[1,*,†] and Hans-Bernd Műhlhaus[2]

[1]*Faculty of Civil and Environmental Engineering, Gdańsk University of Technology, Gdańsk, Poland*
[2]*The University of Queensland St Lucia, Australia*

SUMMARY

A quasi-static homogeneous drained triaxial compression test on cohesionless sand under constant lateral pressure was simulated using a three-dimensional discrete element method. Grains were modelled by means of particle clusters composed of rigid spheres or spheres with contact moments imitating irregular particle shapes. Attention was paid to the effect of initial void ratio and grain shape mixture on the shear strength, volume changes, force chains, kinetic, elastic and dissipated energies. In addition, the effect of the mean grain size, grain size distribution, grain size range, specimen size and roughness and stiffness of boundaries was numerically analysed in initially dense sand. Some numerical results were compared with available experimental results. Copyright © 2014 John Wiley & Sons, Ltd.

1. INTRODUCTION

Because the micromechanical behaviour and fabric properties of granular materials are inherently discontinuous, heterogeneous and nonlinear [1], the application of the discrete element method (DEM), where each grain is modelled individually, has immediate physical appeal. These models directly simulate material micro-structure and thus may be used to comprehensively study different micro-structural events during initiation, growth and formation of shear zones, which strongly affect the macro-properties of granular matter. Their disadvantages are high computational cost, inability to model grain shape accurately and difficulty to validate it experimentally as the inertial and damping effects lose their meaning in quasi-static problems. However, DEM has become more and more popular nowadays for modelling granular materials because of an increasing speed of computers, a connection to the finite element method [2], its usefulness in many multi-scale approaches [3] and a realistic reproduction of micro-scale phenomena such as vortices, periodic volume changes, micro-bands, and force chains [4–7] observed in experiments [8, 9]. To resemble the real grain shape, two main approaches are usually used in DEM: (i) contact moments between rigid spheres or discs are assumed [10–15] or (ii) clusters of combined discrete elements that form irregularly shaped grains are introduced [16–22].

The objective of this paper is to report the results of DEM analyses for a quasi-static drained homogeneous triaxial compression test for cohesionless sand, which is the most important geotechnical laboratory test. The effect of initial void ratio (high and low) and grain shape mixture was studied using discrete clusters of spheres and a linear contact model. The effect of the mean grain size, linear grain size distribution, grain size range width, specimen size and roughness and stiffness of boundaries was

*Correspondence to: J. Tejchman, Faculty of Civil and Environmental Engineering, Gdańsk University of Technology, Gdańsk, Poland.
†E-mail: tejchmk@pg.gda.pl

numerically analysed in initially dense sand using spheres with contact moments and linear contact model in order to significantly decrease the computation time. A three-dimensional (3D) discrete model YADE developed at the University of Grenoble was used [12, 23]. The particle breakage was not considered. The discrete parameters were compared with corresponding experimental data from drained axisymmetric triaxial compression tests performed by Wu [24] at Karlsruhe University with real sand (so-called Karlsruhe sand). All numerical results were shown for one confining pressure. The effect of various confining pressures and initial void ratios on the triaxial compression behaviour of sand with rigid walls (being in a satisfactory agreement with experiments) was studied by DEM in our earlier publications [25, 26]. The behaviour of sand without shear localization was studied because of specimen's dimensions and boundary conditions assumed in experiments. A comprehensive DEM analysis of a homogeneous compression test is also of major importance because this test is (or should be) a main calibration basis of all discrete models for soils. Series of homogenous triaxial compression tests have been simulated by 3D DEM with rigid walls [12, 13, 16], a flexible membrane [27] or a periodic cell [28, 29]. However to our knowledge, comprehensive numerical analyses have not been performed yet, for example, by analysing the effect of the grain shape, stiffness of vertical boundaries and showing the energy evolution and distribution of force chains, porosity and displacement fluctuations. For discrete simulations of sand including shear localization, the reader is referred to our other papers [6, 7, 15].

2. DISCRETE 3D MODEL

To simulate the behaviour of real sand, a 3D spherical discrete model YADE was developed at the University of Grenoble [12, 23] by taking advantage of the so-called soft-particle approach
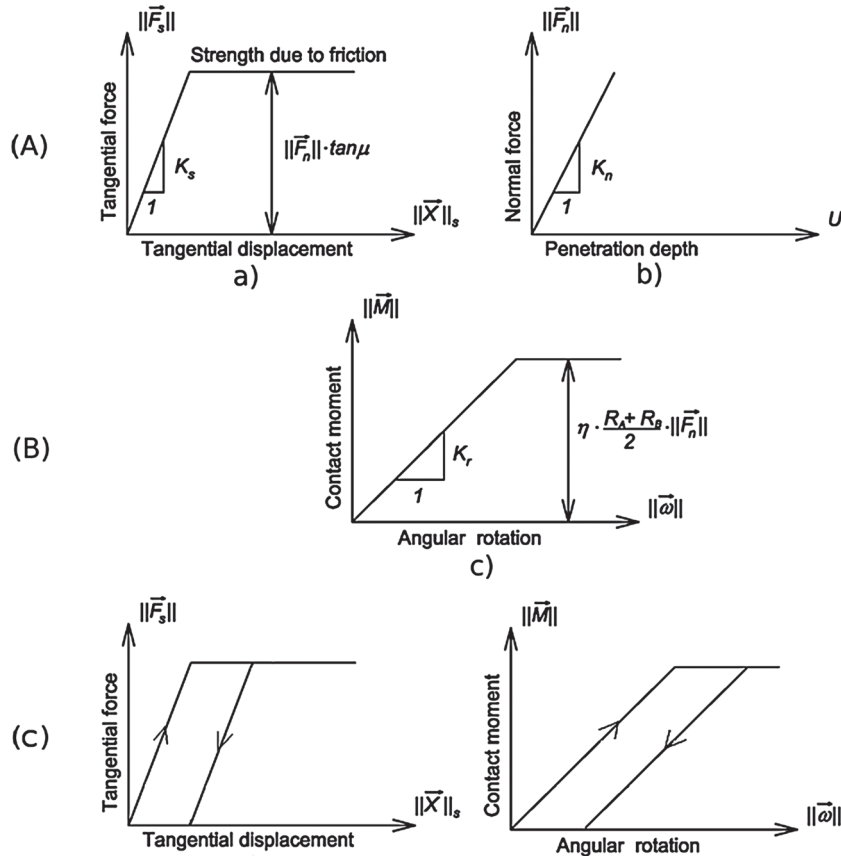

Figure 1. Mechanical response of linear contact model without (A) and with contact moments (B): (a) tangential contact model, (b) normal contact model and (c) rolling contact model [24, 25]; (C) loading and unloading path (tangential and rolling contact).

(i.e. the model allows for particle deformation, which is modelled as an overlap of particles). A linear contact model was used only. A choice of a very simple linear elastic normal contact was intended to capture in average various contact possibilities possible in real sand. The normal and tangential forces were linked to the displacements through the normal stiffness K_n and tangential stiffness K_s (Figure 1A)

$$\vec{F}_n = K_n U \vec{N} \tag{1}$$

$$\vec{F}_s = \vec{F}_s + \Delta \vec{F}_s \ \text{ with } \ \Delta \vec{F}_s = K_s \Delta \vec{X}_s \tag{2}$$

where U is the penetration depth between discrete elements, $\vec{N}$ denotes the unit normal vector at the contact point and $\Delta \vec{X}_s$ is the incremental tangential displacement vector. The unloading was assumed to be purely elastic (Figure 1C). The stiffness parameters were calculated with the aid of the modulus
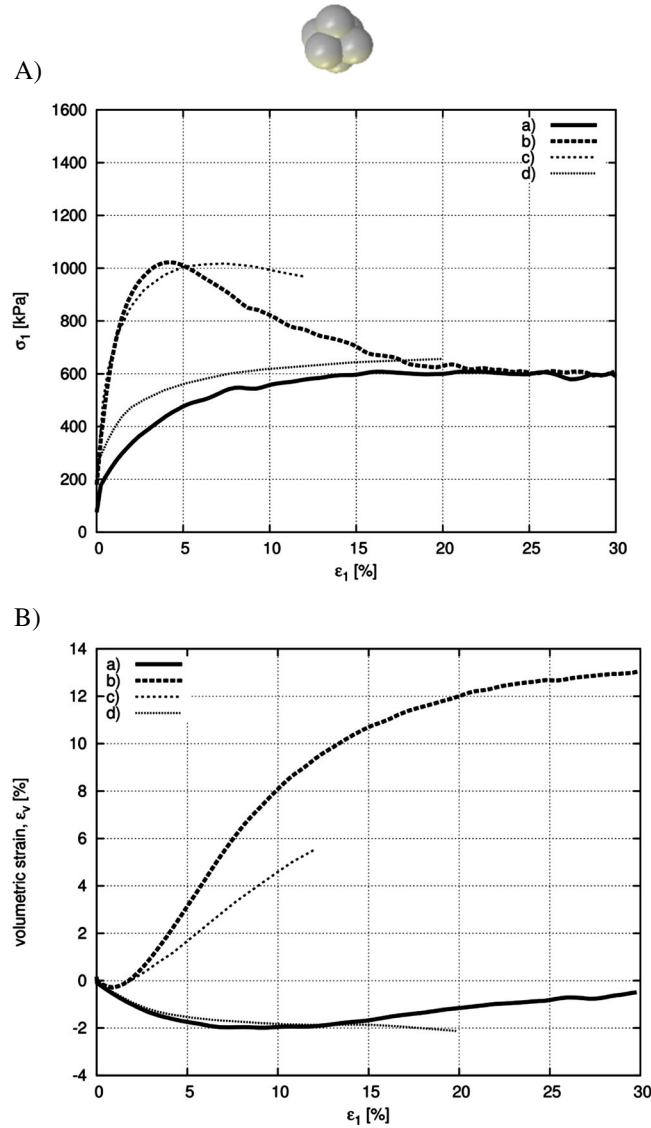

Figure 2. Effect of initial void ratio on vertical normal stress σ_1 versus vertical normal strain ε_1 (A) and volumetric strain ε_v versus vertical normal strain ε_1 (B) from discrete simulations with symmetric clusters composed of six spheres and rigid walls ($E_c = 0.3$ GPa, $v_c = 0.3$, $\mu = 30°$) compared with experiments (curves 'c' and 'd' [21]) during homogeneous triaxial compression test ($\sigma_c = 200$ kPa, $d_{50} = 5.0$ mm): $e_o = 0.79$ (curve 'a') and $e_o = 0.53$ (curve 'b').

of elasticity of the grain contact E_c and two neighbouring grain radii R_A and R_B (to determine the normal stiffness K_n) and with the aid of the modulus of elasticity E_c and Poisson's ratio v_c of the grain contact, and grain radii R_A and R_B (to determine the tangential stiffness K_s) of two neighbouring spheres, respectively [25],

$$K_n = E_c \frac{2\,R_A R_B}{R_A + R_B} \quad \text{and} \quad K_s = v_c\,E_c\,\frac{2\,R_A R_B}{R_A + R_B} \tag{3}$$

If the grain radius $R_A = R_B = R$, the stiffness parameters are equal to $K_n = E_c\,R$ and $K_s = v_c\,E_c\,R$ (thus, $K_s/K_n = v_c$), respectively. The frictional sliding started at the contact point when the contact forces $\vec{F}_s$ and $\vec{F}_n$ satisfied a frictional Mohr–Coulomb equation (Figure 1a)
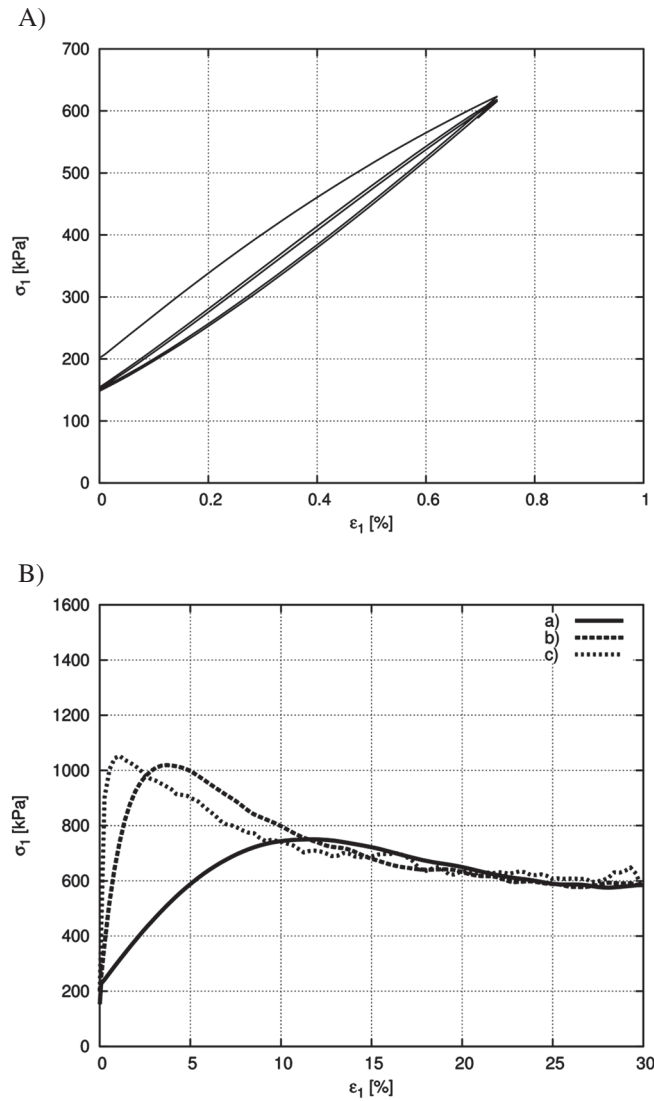
A)

B)

Figure 3. Digital elevation model results for homogeneous triaxial compression test with rigid walls ($\sigma_c = 200$ kPa, $d_{50} = 5.0$ mm, $e_o = 0.53$) and symmetric clusters composed of six spheres ($E_c = 0.3$ GPa, $v_c = 0.3$, $\mu = 30°$): (A) evolution of vertical normal stress σ_1 against vertical normal strain ε_1 in range of $\varepsilon_1 = 0$–0.7% and (B) effect of modulus of elasticity of the grain contact E_c on curve $\sigma_1 = f(\varepsilon_1)$: (a) $E_c = 3$ GPa, (b) $E_c = 0.3$ GPa and (c) $E_c = 0.03$ GPa.

$$\left\| \vec{F}_s \right\| - \left\| \vec{F}_n \right\| \times \tan \mu \le 0 \tag{4}$$

with μ as the inter-particle friction angle (tension was not allowed). No forces were transmitted when grains are separated. The elastic contact constants were specified from the experimental data of a triaxial compression sand test and could be related to the modulus of elasticity of grain material E and its Poisson ratio v [25, 26].

In order to increase the rolling resistance of pure spheres, clusters of spheres or contact moments were introduced [14]. The normal force was assumed to contribute to the rolling resistance. The contact moment increments were calculated by means of the rolling stiffness K_r multiplied with the angular rotational increment vectors $\Delta \vec{\omega}$ (Figure 1B)

$$\Delta M = K_R \times \Delta \vec{\omega}. \tag{5}$$

The rolling stiffness K_r (kNm) in Eq. 5 was related to the tangential stiffness K_s (kN/m) in Eq. 2 by the following formula proposed by Iwashita and Oda [10]

$$K_R = \beta \times K_s \times R^2 = \beta \times K_s \times R_A R_B, \tag{6}$$

where β is the dimensionless rolling stiffness coefficient and R is the grain radius (at small displacements $dX_r \approx dX_s$). The dimensionless rolling coefficient η controlled the limit friction moment of the rolling behaviour

$$\left\| \vec{M} \right\| - \eta \frac{R_A + R_B}{2} \left\| \vec{F}_n \right\| \le 0. \tag{7}$$

To dissipate excessive kinetic energy in the discrete system, a simple local non-viscous damping scheme was adopted [30], which assumed a change of forces and moment by using the damping parameter α

$$\vec{F}_{damped}^{k} = \vec{F}^{k} - \alpha \cdot \text{sgn}\left(\vec{v}^{k} \right) \left| \vec{F}^{k} \right|, \tag{8}$$

$$\vec{M}_{damped}^{k} = \vec{M}^{k} - \alpha \cdot \text{sgn}\left(\vec{\omega}^{k} \right) \left| \vec{M}^{k} \right| \tag{9}$$

where $\vec{F}^{k}$ and $\vec{M}^{k}$ are the kth components of the residual force and moment vector and $\vec{v}^{k}$ and $\vec{\omega}^{k}$ are the kth components of the translational and rotational velocity. A positive damping coefficient α is smaller than 1
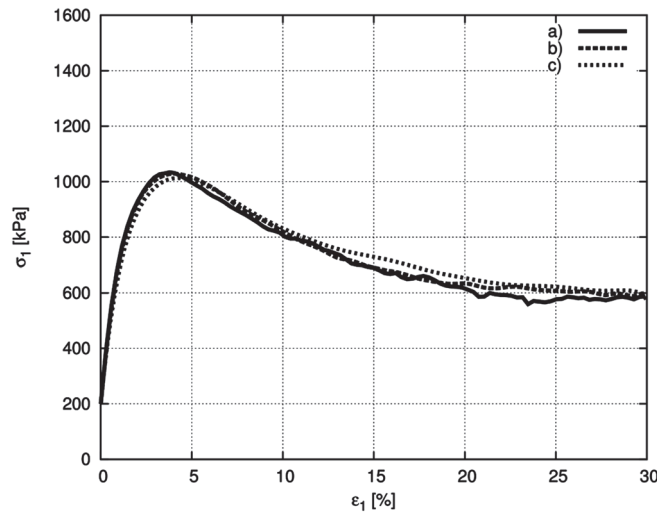

Figure 4. Effect of loading velocity v on vertical normal stress σ_1 versus vertical normal strain ε_1 from discrete simulations of homogeneous triaxial compression test with rigid walls ($\sigma_c = 200$ kPa, $d_{50} = 5.0$ mm, $e_o = 0.53$) and symmetric clusters composed of six spheres ($E_c = 0.3$ GPa, $v_c = 0.3$, $\mu = 30°$): (a) $v = 100$ mm/s, (b) $v = 10$ mm/s and (c) $v = 1$ mm/s.

(sgn(•) returns the sign of the kth component of velocity). The equations are separately applied to each kth component of a 3D vector x, y and z. Note that the effect of damping is insignificant in quasi-static calculations.

The following local material parameters were needed for discrete simulations model: E_c, v_c and μ (when using clusters) and E_c, v_c, μ, β and η (when using spheres with contact moments).
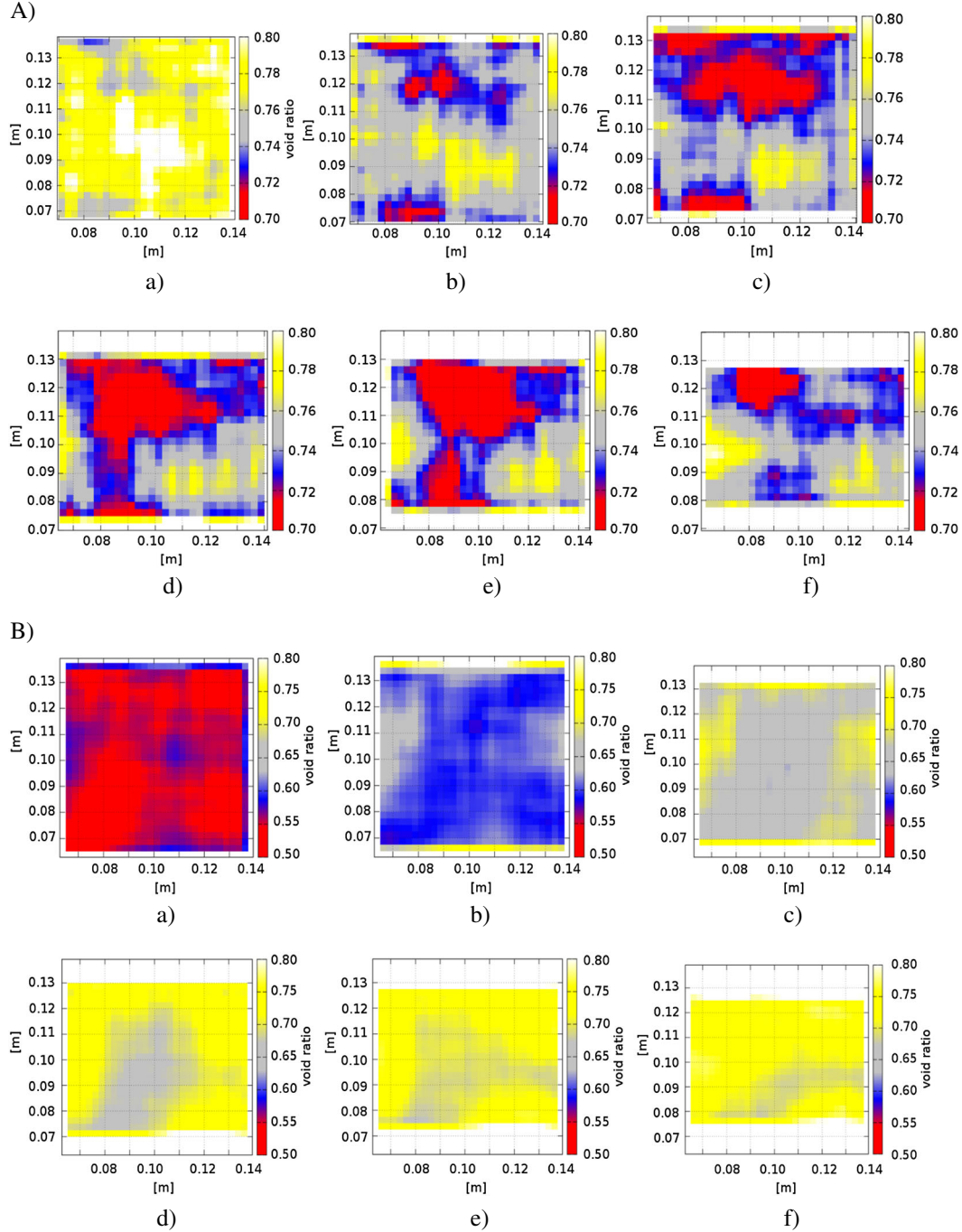

Figure 5. Distribution of void ratio in vertical mid-section of thickness d_{50} in (A) initially loose ($e_o = 0.79$) and (B) initially dense ($e_o = 0.53$) sand specimen at (a) $\varepsilon_1 = 0\%$, (b) $\varepsilon_1 = 5\%$, (c) $\varepsilon_1 = 10\%$, (d) $\varepsilon_1 = 15\%$, (e) $\varepsilon_1 = 20\%$, and (f) $\varepsilon_1 = 25\%$; (C) evolution of mean void ratio and standard deviation of e (a) $e_o = 0.79$ and (b) $e_o = 0.53$ from discrete simulations with symmetric clusters composed of six spheres ($E_c = 0.3$ GPa, $v_c = 0.3$, $\mu = 30°$) during homogeneous triaxial compression test with rigid walls ($\sigma_c = 200$ kPa, $d_{50} = 5.0$ mm).

In addition, the particle radius R, particle mass density ρ and damping parameter α were required.

The discrete material parameters were calibrated with the aid of corresponding axisymmetric triaxial laboratory test results on Karlsruhe sand by Wu [24] and Kolymbas and Wu [31] by comparing the macroscopic stress–strain and volume–strain evolution curves for different pressures and initial void ratios [26]. The specimen height and diameter were assumed purposively to be equal both to 100 mm in order to inhibit a shear localization process. After laboratory tests, the deformed specimens had always a form of the so-called elephant's foot because of gravity. The index properties of Karlsruhe sand are [32] mean grain diameter $d_{50} = 0.50$ mm, grain size among 0.08 and 1.8 mm, uniformity coefficient $U = d_{60}/d_{10} = 2$, maximum specific weight $\gamma_d^{max} = 17.4$ kN/m³, minimum void ratio $e_{min} = 0.53$, minimum specific weight $\gamma_d^{min} = 14.6$ kN/m³ and maximum void ratio $e_{max} = 0.84$. The sand grains may be classified as sub-rounded/sub-angular.

In numerical simulations, a cubical sand specimen of $10 \times 10 \times 10$ cm³ was mainly used. The tests were modelled mainly using confining smooth rigid wall elements to induce homogeneous deformation [12, 13, 16]. This assumption was justified because of the lack of shear localization in real tests (Section 3.3). The frictionless top and bottom boundaries moved vertically as loading platens under strain-controlled conditions to simulate the confining pressure p. The loading speed
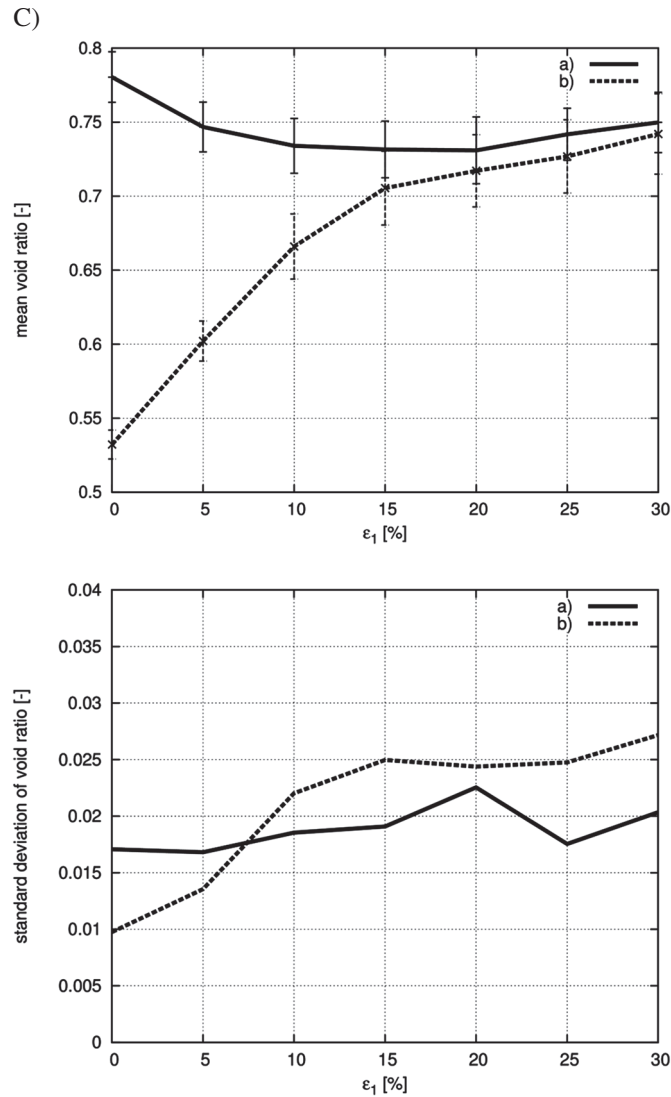
C)

Figure 5. (Continued).

was slow enough (10 mm/s) to ensure the test was conducted under quasi-static conditions (Figure 4). A simplified linear grain distribution curve was assumed for Karlsruhe sand (the grain size range was mainly 2.5–7.5 mm with $d_{50} = 5$ mm). Each granular assembly was prepared by putting clusters of spheres (or spheres) of a random radius according to the grain distribution curve (without gravity) into a cubical container with six external walls, which had a regular cubical grid with a particle distance of 10 mm. In order to obtain a desired initial density owing to grain overlapping, the inter-particle friction coefficient was varied between $0°$ and μ (initially dense sand) and between $0°$ and $89°$ (initially loose specimen) to exactly reproduce the target initial sand volumetric weight. During dynamic compression to the desired confining pressure σ_c, grains bounced against each other and moved in random directions; thus, their initial ordered arrangement became random. The assembly was then allowed to settle to a state where the kinetic energy was negligible and then friction coefficient was set to the target inter-particle friction angle μ. The isotropic assembly was then subjected to the boundary driven triaxial compression. The histogram of the contact orientation showed that all contacts were homogeneously distributed in all directions prior to deformation. It has to be noted that after the sample was generated with the inter-particle friction angle higher than
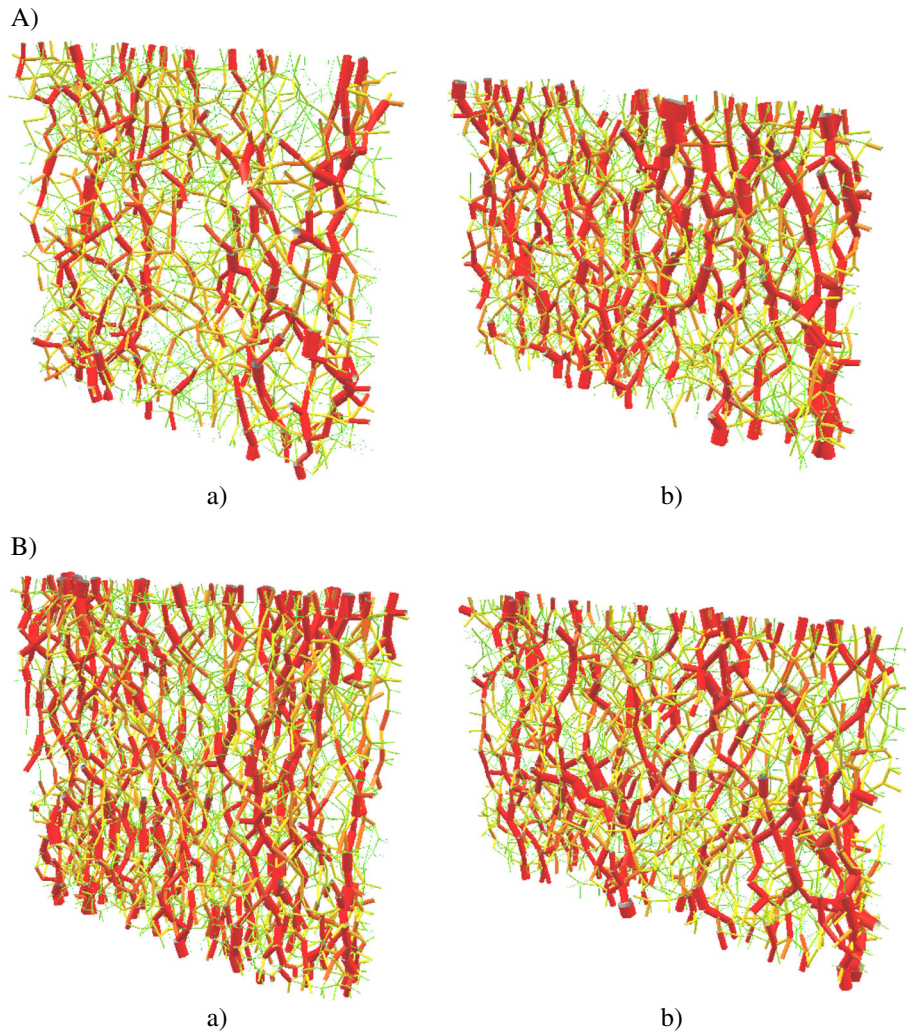

Figure 6. Distribution of internal forces at vertical mid-section with thickness of 2 cm, right at vertical normal strain $\varepsilon_1 = 5\%$ (a) and $\varepsilon_1 = 25\%$ (b) from discrete simulations with symmetric clusters composed of six spheres ($E_c = 0.3$ GPa, $v_c = 0.3$, $\mu = 30°$) during homogeneous triaxial compression test with rigid walls ($\sigma_c = 200$ kPa, $d_{50} = 5.0$ mm): (A) initially loose sand ($e_o = 0.53$) and (B) initially dense sand ($e_o = 0.53$) (red colour – force ≥ 20 N, orange and yellow colour – force >0 N and <20 N).

the target one, some contact forces were outside the Coulomb cone defined by the target friction angle. Hence, an initial collapse of the specimen occurred connected with the difficulty of producing initial loose states. On the other hand, after the sample was generated with the inter-particle friction angle smaller than the target one, initial states with artificially large initial coordination numbers might occur [33–35].

In addition, flexible vertical walls were assumed to model the membrane surrounding the specimen in experiments. They were composed of linked overlapping rigid spheres of the diameter of $1.1 \times d_{50}$ arranged into a flat triangular grid (their stiffness was equal to 0.01 of the stiffness of sand spheres with $\mu = 0$). The membranes were allowed to freely move to mimic the specimen deformation, independent of neighbouring membrane elements. In order to induce constant lateral pressure, each membrane was divided into eight separate parts along the height. The forces acting on membrane spheres were independently calculated in each part. Note that DEM calculations with vertical non-rigid walls lasted longer by the factor 3 than those with rigid walls.

3. DISCRETE RESULTS OF HOMOGENEOUS TRIAXIAL COMPRESSION TEST

3.1. Effect of initial void ratio

The exemplary calculations were carried out with a symmetric cluster composed of six rigid spheres [26]. The following discrete material parameters were used in simulations: $E_c = 300$ MPa, $v_c = 0.3$, $\mu = 30°$, $\rho = 2.6$ g/cm^3, $\alpha = 0.08$ and $d_{50} = 5.0$ mm to match approximately experimental macroscopic results for real sand with $d_{50} = 0.5$ mm in the range of different confining pressures (e.g. $\sigma_c = 200$ kPa and $\sigma_c = 500$ kPa) at $e_o = 0.53$ [12, 26]. The linear grain range was among 2.5 and 7.5 mm. The aspect index a and the convexity indexes c_1 and c_2 of the cluster were $a = 1.0$, $c_1 = 1.67$ and $c_2 = 1.14$, respectively. The aspect index a was defined as the ratio between the maximum and minimum cluster diameter, the convexity index c_1 as the ratio between the smallest sphere volume encompassing the cluster and the cluster volume, and the convexity index c_2 as the ratio between the smallest convex volume encompassing the cluster and the cluster volume [26]. About 11,000 symmetric clusters were used with 66,000 spheres. The computation CPU time was 3 days using PC 3 GHz.

Figure 2 shows the calculated evolution of the vertical normal stress σ_1 and volumetric strain ε_v versus the vertical normal strain ε_1 for a symmetric cluster of six spheres during triaxial compression with initially loose ($e_o = 0.79$, $d_{50} = 5$ mm) and initially dense sand ($e_o = 0.53$, $d_{50} = 5$ mm) under one confining pressure ($\sigma_c = 200$ kPa) as compared with the laboratory experiments by Wu [24]. The
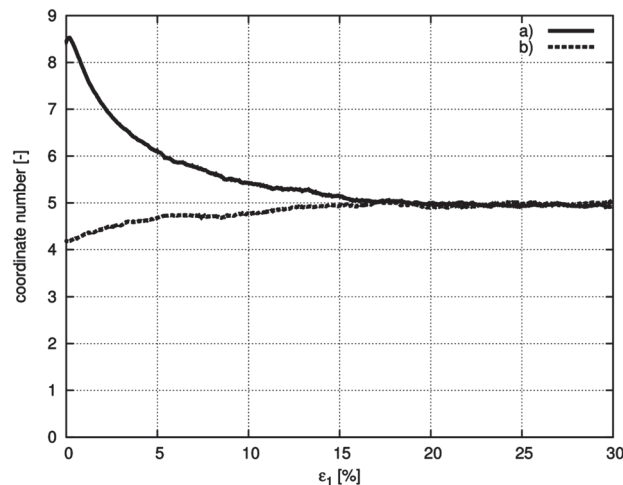

Figure 7. Evolution of coordination number from discrete simulations with symmetric clusters composed of six spheres ($E_c = 0.3$ GPa, $v_c = 0.3$, $\mu = 30°$) during homogeneous triaxial compression test with rigid walls ($\sigma_c = 200$ kPa, $d_{50} = 5.0$ mm): (a) initially dense sand ($e_o = 0.53$) and (b) initially loose sand ($e_o = 0.79$).

results follow from one arbitrary numerical simulation for each e_o. A loose configuration with $e_o \leq 0.75$ could be consistently achieved only. A looser configuration could not be obtained because of a collapse of the pore space under σ_c.

Similar to real experiments, the initially dense specimen exhibits initial elasticity, and then hardening (connected first to contractancy and then dilatancy), reaches a peak strength at about of $\varepsilon_1 = 3$–6%, and gradually softens and dilates reaching at large vertical strain of 25–30% a critical state [13, 16]. The calculated global macroscopic elastic parameters are $E = 65$ MPa and $v = 0.25$. The global modulus of elasticity was determined based on the inclination of the initial stress–strain curve during loading ($E = 67$ MPa) and the mean inclination of the initial stress–strain curve during
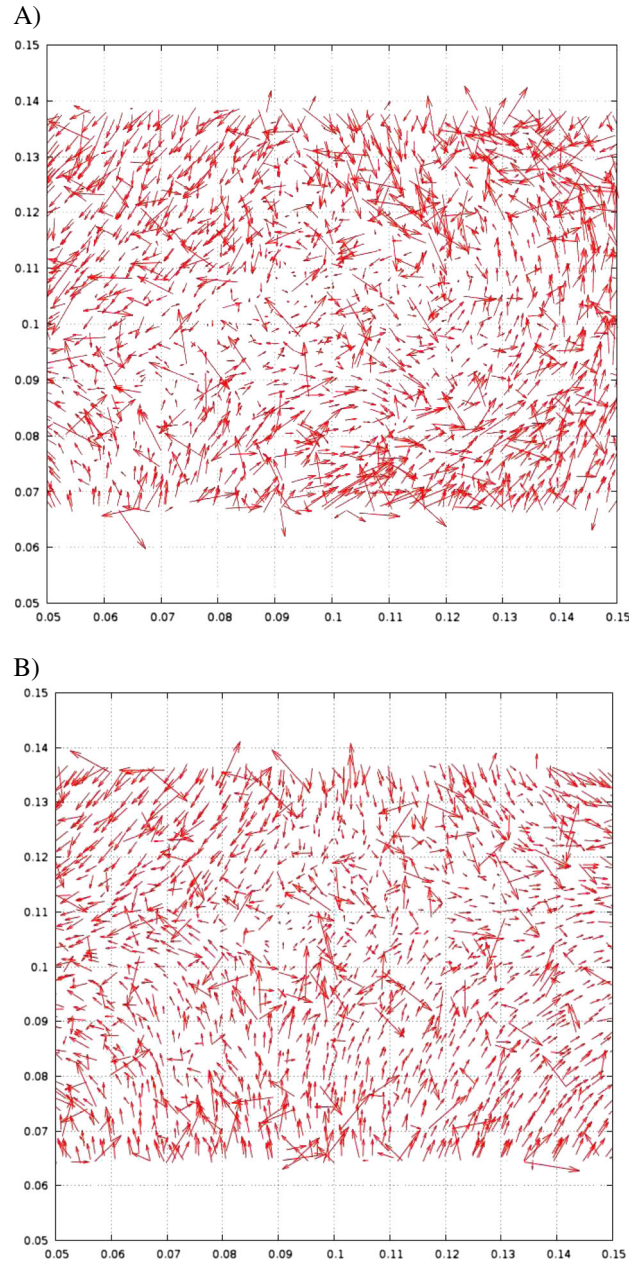
A)

B)

Figure 8. Maps of displacements fluctuations in specimens from discrete simulations with symmetric clusters composed of six spheres ($E_c = 0.3$ GPa, $v_c = 0.3$, $\mu = 30°$) during homogeneous triaxial compression test with rigid walls ($\sigma_c = 200$ kPa, $d_{50} = 5.0$ mm) at $\varepsilon_1 = 25\%$: (a) initially loose sand ($e_o = 0.79$) and (b) initially dense sand ($e_o = 0.53$).

unloading and reloading ($E = 63$ MPa) (Figure 3A). The global elastic modulus of $E = 65$ MPa estimated from the stress–strain curve is smaller than that deduced from the elastic wave velocity in the granular specimen $E = \frac{v_f^2 \rho (1+v)(1-2v)}{1-v} = 100$ MPa (with $\rho = 2.6$ g/cm^3, $v = 0.25$ and mean wave velocity $v_f \approx 200$ m/s from DEM). The higher the E_c, the larger the E, in particular if $E_c << 0.3$ GPa (Figure 3B). The calculated E is smaller than the experimental one of $E = 100$ MPa. Thus, the assumed parameter E_c should be higher. However, a change of E_c affects also other material parameters that require a re-calibration process. It has to be noted that the strain–strain curve is very sensitive to the increasing contact stiffness because of artificially high coordination numbers in an initially dense packing [33–35]. The global maximum mobilised internal friction angle (calculated with principal stresses from the Mohr's equation $\phi = \arcsin[(\sigma_1 - \sigma_2)/(\sigma_1 + \sigma_2)]$, where σ_i are the principal stresses ($\sigma_2 = \sigma_c$)) is $\phi_{max} = 43.1°$ and indicates a good similarity to the experimental value of $\phi_{max} = 42°$. The calculated strain $\varepsilon_1 = 3\%$ corresponding to the peak stress is about twice smaller as compared with laboratory tests (slightly influenced by a stochastic distribution). The calculated dilatancy angle of $\psi = 40°$ is too high as compared with the experimental value ($\psi = 28.5°$) (the mobilised dilatancy angle ψ was computed as $\psi = \arctan(d\varepsilon_v/d\varepsilon_1)$). The calculated global residual internal friction angle is $\phi_{cr} = 30°$. The calculated stress–strain curve does not depend on the prescribed loading speed v (Figure 4).

The initially loose specimen exhibits initial elasticity and then hardening connected to strong contractancy and small dilatancy at $\varepsilon_1 > 10\%$ approaching a critical state (similar to real experiments [24]). The unexpected dilatancy at large deformation is caused by the fact that the assembling
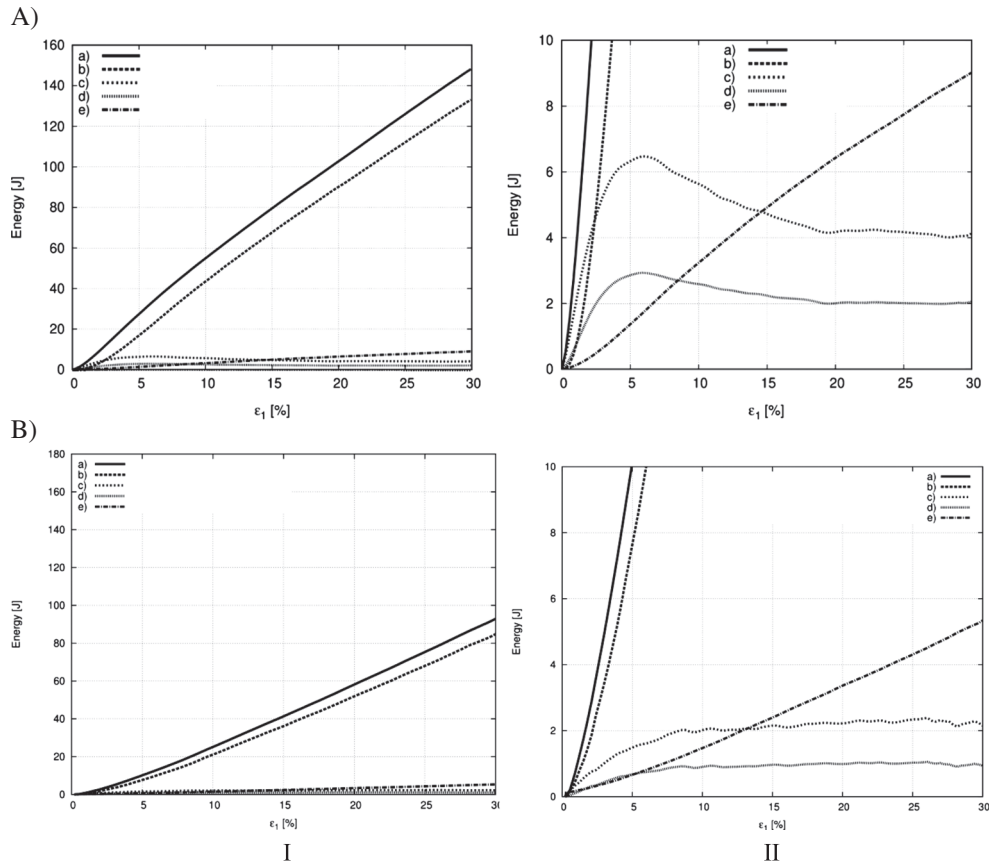

Figure 9. Calculated evolution of (a) total energy E, (b) plastic dissipation D_p, (c) elastic energy in normal direction E_c^n, (d) elastic energy in tangential direction E_c^s and (e) numerical non-viscous damping D_n during homogeneous triaxial compression test ($\sigma_c = 200$ kPa, $d_{50} = 5.0$ mm) with symmetric clusters of six spheres: (A) $e_o = 0.53$ and (B) $e_o = 0.76$ (I) wide view, (II) zoom.

procedure was unable to produce very loose specimens. The global macroscopic elastic parameters are $E = 60$ MPa (similar to the experiment) and $\nu = 0.25$. The calculated global residual internal friction angle is $\phi_{cr} = 30°$ (similar as in the case with $e_o = 0.53$). The calculated contractancy angle of $\psi = -10°$ is the same as the experimental outcome.

Summing up, we may conclude that both experimental curves are satisfactorily reproduced in discrete simulations of initially loose and dense sand in spite of the fact that the real grain shape, mean grain size and grain size distribution of Karlsruhe sand were not taken into account and the assembling procedure was unable to produce really loose specimens and provided too high coordination numbers in dense specimens. The results have shown that the grain shape turned out to be a very influencing parameter in discrete simulations [26] (Figs. 15 and 16).

The effect of initial void ratio on the distribution of void ratio during deformation in a vertical specimen mid-section of the thickness d_{50} is shown in Figs. 5A and 5B. The sectional void ratio was calculated from the cell of $5d_{50} \times 5d_{50}$ moved by the distance equal to d_{50}. The distribution of void ratio is always non-uniform during the entire deformation process. It depends strongly on a stochastic distribution of discrete element (thus, a non-affine displacement field correlation length
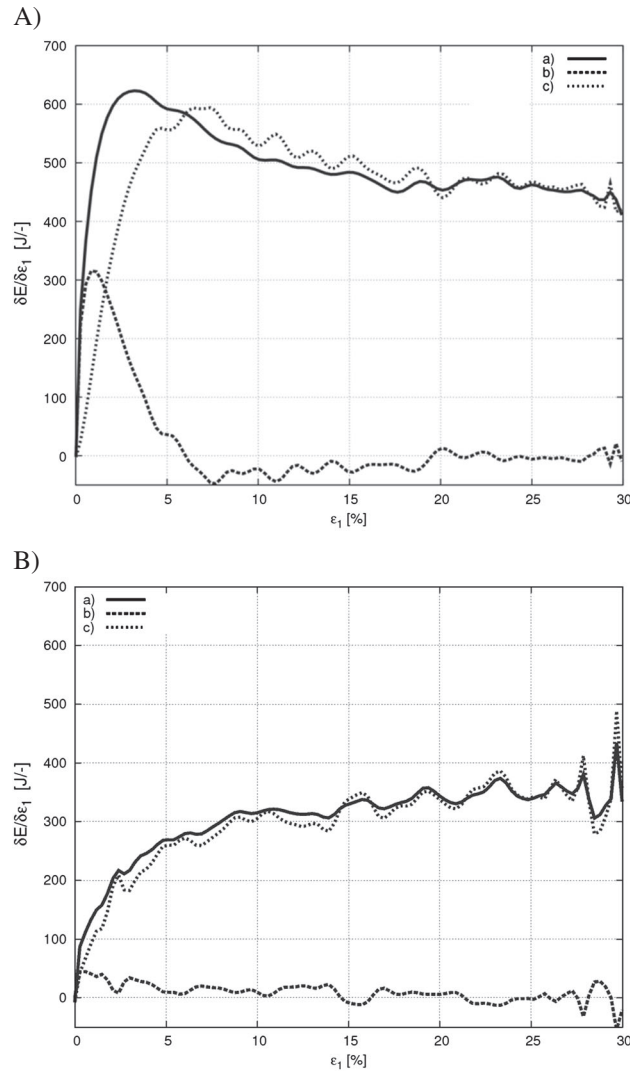

Figure 10. Calculated evolution of (a) external energy derivative δE with respect to vertical normal strain ε_1 ($\delta E/\delta\varepsilon_1$), (b) elastic internal energy derivative $\delta E_e/\delta\varepsilon_1$ and (c) plastic dissipation derivative $\delta D_p/\delta\varepsilon_1$ during homogeneous triaxial compression test ($\sigma_c = 200$ kPa, $d_{50} = 5.0$ mm) with symmetric clusters of six spheres: (A) $e_o = 0.53$ and (B) $e_o = 0.76$.

could not be found). The void ratio changes in a vertical mid-section at $\varepsilon_1 = 25\%$ are between 0.70 and 0.79 (initially loose sand) and between 0.65 and 0.75 (initially dense sand). The standard deviation of void ratio variance in a vertical mid-section (which can be interpreted as a variance of a local density field) (Figure 5C) is initially weaker and then stronger (at $\varepsilon_1 > 7\%$) in initially dense sand.

Figure 6 demonstrates the distribution and size of the contact network in the specimen. The red colour lines with a different thickness represent the magnitude of compressive normal contact forces between two particles larger than 20 N. The distribution of internal contact forces is non-uniform and continuously changes [5, 6, 19, 36–38]. Force chains of heavily loaded grain contacts bear and transmit the compressive load on the entire granular system and are the predominant structure of internal forces at micro-scale. The contact number is significantly higher in an initially dense specimen (36,751 at $\varepsilon_1 = 5\%$ and 30,323 at $\varepsilon_1 = 25\%$) than in an initially loose specimen (24,219 at $\varepsilon_1 = 5\%$ and 25,713 at at $\varepsilon_1 = 25\%$) (Figure 6) because of a lower void ratio. It decreases in initially dense sand during deformation because of dilatancy and increases in initially loose one because of contractancy. The magnitude of contact forces may be even higher in initially loose sand. The coordination number (expressed by the average number of contacts per particle) decreases during deformation in initially dense sand (from 8.5 down to 5) because of dilatancy (Figure 7). For initially loose sand, the coordination number increases from 4.5 up to 5 because of contractancy (Figure 7).

In both specimens, the so-called vortex structures (rigid body rotating systems corresponding to displacement fluctuations [5, 6]) do not occur (Figure 8) because of the lack of shear localization. The maps of Figure 8 were obtained by drawing the displacement difference vector for each sphere between $n = 50$ iterations with respect to the background translation corresponding to the homogeneous (affine) strain (the effect of iterations' number n was negligible).

The effect of e_o on the total accumulated energy, elastic internally stored energy at contacts, frictional dissipation and numerical damping in sand ($e_o = 0.53$ or $e_o = 0.79$, $p = 200\,\text{kPa}$, $d_{50} = 5.0\,\text{mm}$) from DEM is demonstrated in Figure 9. The knowledge on the energy evolution is very important in particular in stability problems.

The elastic internal energy stored at contacts N between grains E_e, expressed in terms of work of elastic contact tangential forces F_s on elastic tangential displacements U_s, contact normal forces F_n on elastic penetration depths U and contact moments M on elastic rotations ω (moments were absent where clumps were used) was

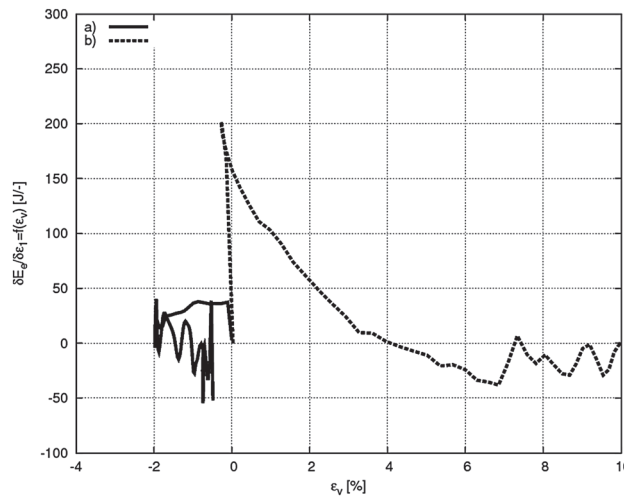$$E_e = \sum_1^N \left(\frac{|F_s^e|^2}{2K_s} + \frac{|F_n|^2}{2K_n} + \frac{|M^e|^2}{2K_r} \right) \tag{10}$$

Figure 11. Calculated initial evolution of elastic internal energy derivative δE_e during homogeneous triaxial compression test with respect to vertical normal strain as $\delta E_e / \delta \varepsilon_1 = f(\varepsilon_v)$ with symmetric clusters of six spheres: (a) $e_o = 0.79$ and (b) $e_o = 0.53$ ($\sigma_c = 200\,\text{kPa}$, $d_{50} = 5.0\,\text{mm}$).

The kinetic energy E_k of grains was caused by their translation and rotation

$$E_k = \sum_1^N \left(\frac{1}{2}mv^2 + \frac{1}{2}I\dot{\omega}^2 \right) \tag{11}$$

where m is the mass and I denotes the moment of inertia of a particle (v – translational velocity, $\dot{\omega}$ – rotational velocity).

The dissipated energy D_p, expressed in terms of work of the tangential (shear) forces on conjugate sliding displacements and moments on conjugate rotations was determined as

$$D_p = D_p + \Delta D_p \quad \text{with} \quad \Delta D_p = \sum_1^N F_s^{pl} U_s^{slip} + M^{pl}\omega \ . \tag{12}$$
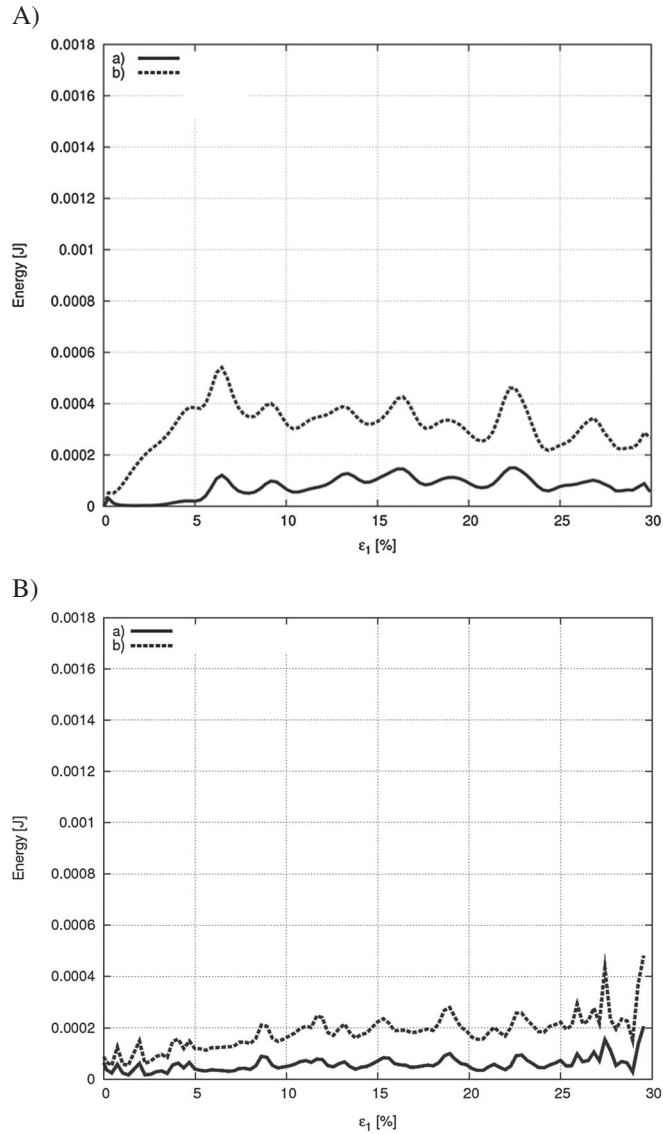
A)

B)

Figure 12. Calculated evolution of kinetic energy E_c during homogeneous triaxial compression test with rigid walls and symmetric clusters of six spheres: (a) rotational kinetic energy, (b) translational kinetic energy, (A) $e_o = 0.53$ and (B) $e_o = 0.76$ ($\sigma_c = 200\,\text{kPa}$, $d_{50} = 5.0\,\text{mm}$).

In addition, the numerical dissipation D_n was specified during translation and rotation (Eqs 8 and 9). The total accumulated energy

$$E = E_e + E_k + D_p + D_n \qquad (13)$$

was equal to the external boundary work W expended on the assembly always by six external normal forces on displacements of six rigid external walls.

The total energy, plastic damping and elastic energy are higher by the factor 2 in initially dense sand. There exists a roughly linear relationship between the total energy and the vertical normal strain ε_1 and between the damping plastic force and ε_1 as a consequence of a residual state (Figure 9). The plastic dissipation during frictional sliding is equal to 80% of the total energy at $\varepsilon_1 = 5\%$. At the residual state of $\varepsilon_1 = 30\%$, it is already equal to 90% of the total energy. The numerical sliding damping is always equal to about 5% of the total energy only (Figure 9II). The evolution of the total elastic internal energy is similar to the evolution of the shear strength. The elastic energy portion due to tangential force action is smaller (about twice) than that due to the normal force action in view of the lack of plastic damping. At the beginning of deformation at $\varepsilon_1 < 1\%$, the total energy is almost fully converted into the elastic energy. The elastic internal work of contact forces is 75% ($e_o = 0.53$) and 80% ($e_o = 0.79$) at $\varepsilon_1 = 1\%$, and 4% ($e_o = 0.53$) and 3% ($e_o = 0.79$) at $\varepsilon_1 = 30\%$ of the total energy, respectively. The elastic energy ratio is the same at the residual state.

The derivative δE_e of the elastic force-internal work with respect to ε_1 ($\delta E_e / \delta \varepsilon_1$) is initially positive (Figure 10). It rapidly approaches zero at about $\varepsilon_1 = 5$–6%. For initially dense sand, it becomes negative (as $E_e = f(\varepsilon_1)$ strongly diminishes) and afterwards approaches an asymptote at zero for both cases (as $E_e = f(\varepsilon_1)$ reaches a residual state). Beyond strains of $\varepsilon_1 = 6\%$ ($e_o = 0.53$) or $\varepsilon_1 = 1\%$ ($e_o = 0.79$), the almost entire input work is dissipated because of plastic deformation and numerical damping (the external energy rate and dissipation rate are equal $\delta W \cong \delta D$). The fluctuations of the energy rates are pronounced in both sands at the residual state.

In an initially dense specimen, the elastic energy rate decreases during a dilative deformation process only (which follows the initial contractive phase at $\varepsilon_1 > 1\%$) (Figure 11). In an initially loose specimen, it continuously decreases during an initial strong contractant phase ($0 < \varepsilon_1 \leq 10\%$) and a following weaker dilatant phase ($\varepsilon_1 > 10\%$) (Figure 11).

In general, the kinetic energy E_k (Eq. 12) is small because of the quasi-static loading of the granular system. The kinetic energy (translational and rotational) is higher for initially dense sand. The translational kinetic energy is always five times higher than the rotational one. The evolution of the transitional ones is similar to the mobilised internal friction evolution. A release of the elastic energy
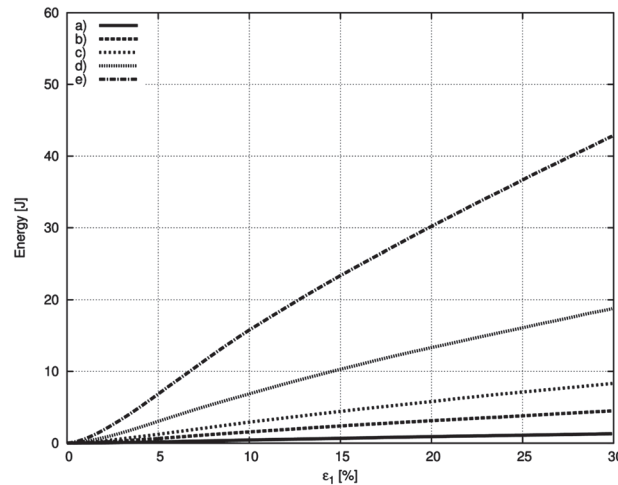

Figure 13. Calculated evolution of numerical damping energy D_n during homogeneous triaxial compression test with rigid walls and symmetric clusters of six spheres for different damping parameter α ($e_o = 0.53$, $\sigma_c = 200$ kPa, $d_{50} = 5.0$ mm): (a) $\alpha = 0.01$, (b) $\alpha = 0.04$, (c) $\alpha = 0.08$, (d) $\alpha = 0.20$ and (e) $\alpha = 0.50$.

induces grain motion. In the elastic stage, the kinetic energy is close to zero. The translational kinetic energy increases up to $\varepsilon_1 = 5\text{–}10\%$ and then decreases with $e_o = 0.53$ or continuously increases with $e_o = 0.79$. The kinetic energy shows fluctuations, which correspond to the evolution of the elastic energy and damping rate (Figure 12).

The effect of the damping coefficient α (Eq. 8) on the damping energy D_n in initially dense sand is shown in Figure 13. The damping energy obviously grows with increasing parameter α. The effect is rather negligible if $\alpha \leq 0.08$ (i.e. the value assumed in calculations).
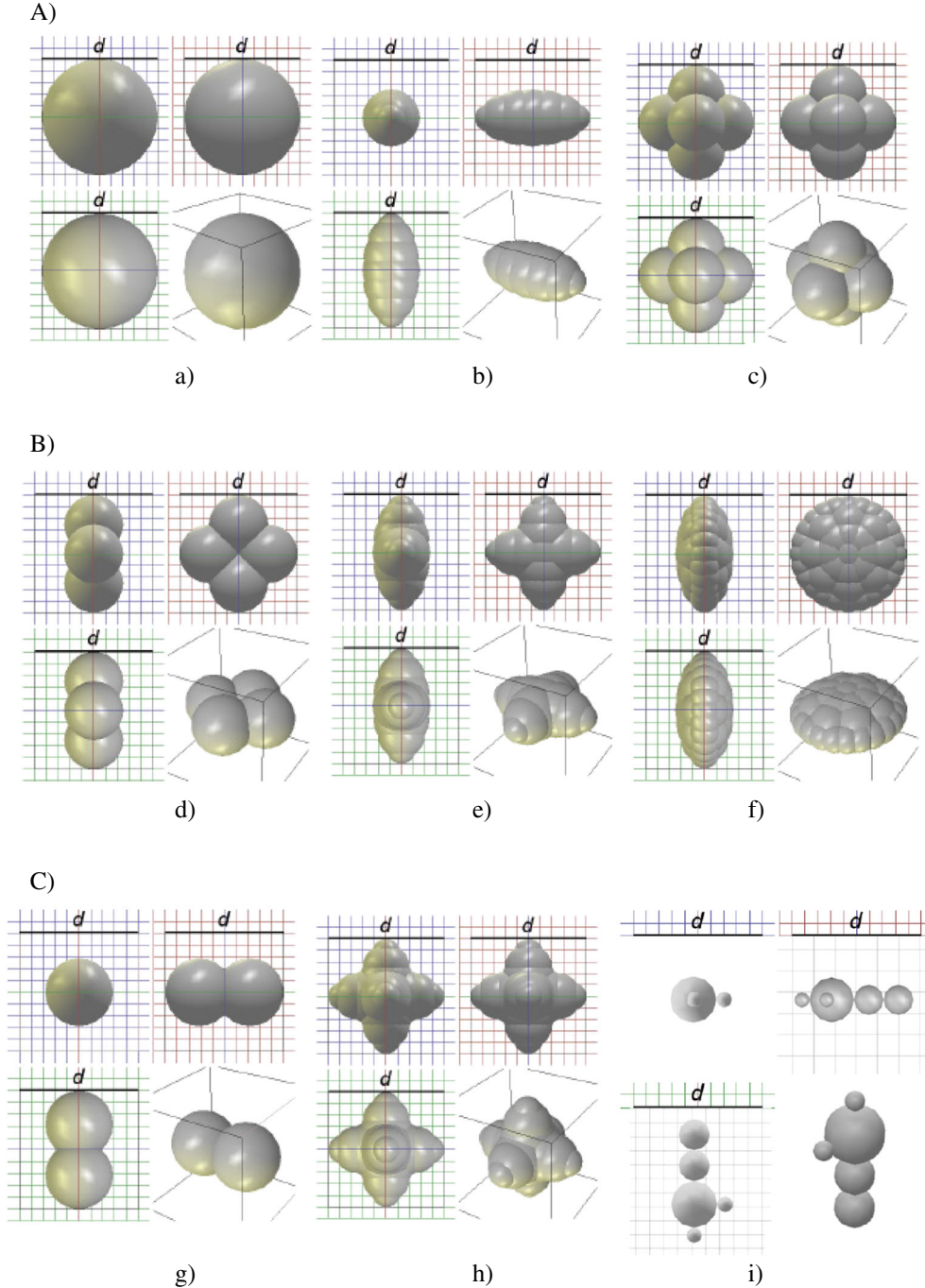

Figure 14. Three different grain shape mixtures ('A'–'C') created by symmetric and non-symmetric clusters of spheres used in discrete simulations of triaxial compression (d – grain diameter).

A)

B)

C)

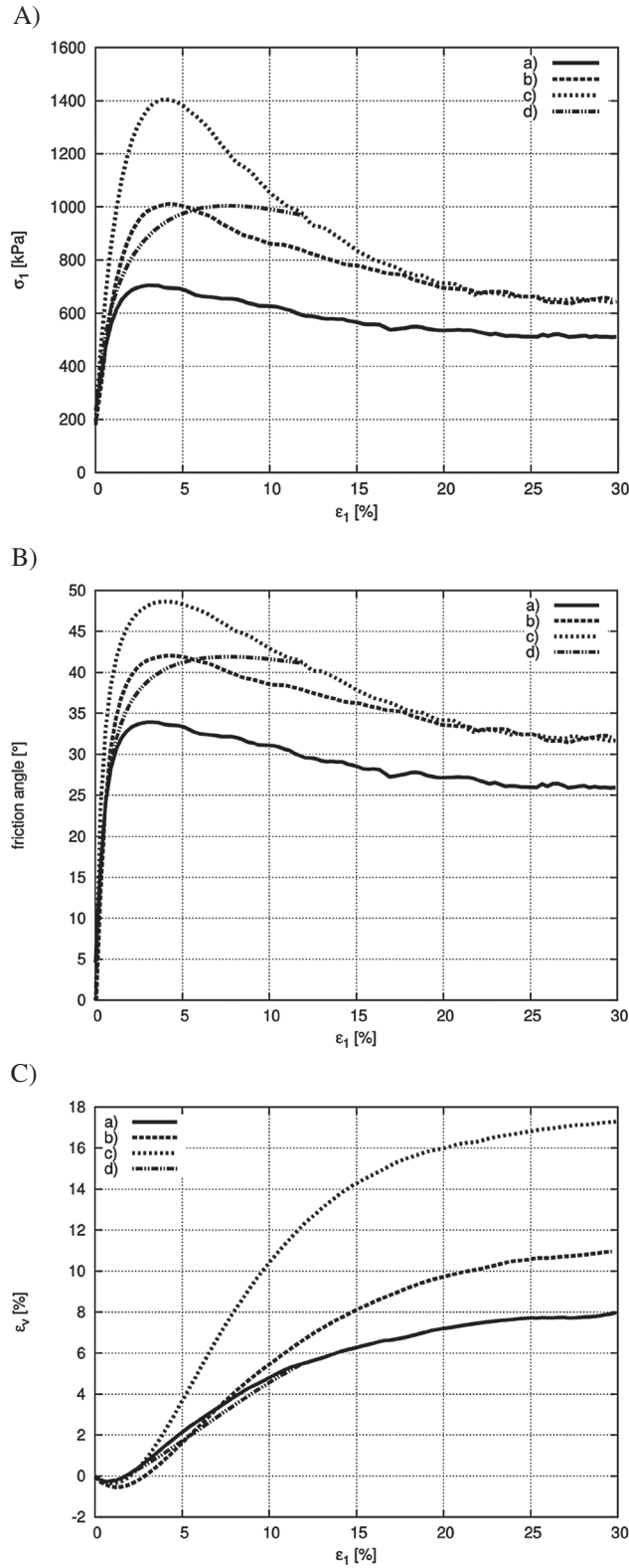Figure 15. Effect of grain shape distribution on vertical normal stress σ_1 versus vertical normal strain ε_1 (A) and volumetric strain ε_v versus vertical normal strain ε_1 (B) from discrete simulations ($E_c = 0.3$ GPa, $v_c = 0.3$, $\mu = 30°$) compared with experiments [23] (curve 'd') during homogeneous triaxial compression test with rigid walls ($e_o = 0.53$, $\sigma_c = 200$ kPa, $d_{50} = 5.0$ mm): curve 'a' – grain shape mixture of Figure 15A, curve 'b' – grain shape mixture of Figure 15B and curve 'c' – grain shape mixture of Figure 15C.

3.2. Effect of grain shape mixture

In order to improve our discrete simulations results, the calculations were carried out with an initially dense specimen only using three different mixtures of grains including three different shapes in the equal proportion 1/3 each (Figure 14). The mixture choice was assumed at random. The same

Table I. The aspect indexes a and convexity indexes c_1 and c_2 for different grain shapes and grain shape mixtures assumed in calculations (Figure 14).

| Type	Aspect index a	Convexity index c_1	Convexity index c_2
Grain shape 'a'	1	1	1
Grain shape 'b'	2	4.15	1.04
Grain shape 'c'	1	1.67	1.14
Grain shape 'd'	2	2.26	1.15
Grain shape 'e'	2	2.95	1.05
Grain shape 'f'	2	2.08	1.03
Grain shape 'g'	1.75	2.81	1.11
Grain shape 'h'	1	2.35	1.2
Grain shape 'i'	2.7	11.93	1.3
Grain shape of mixture 'A' (mean value)	1.33	2.27	1.06
Grain shape of mixture 'B' (mean value)	2	2.43	1.08
Grain shape of mixture 'C' (mean value)	1.81	5.69	1.2
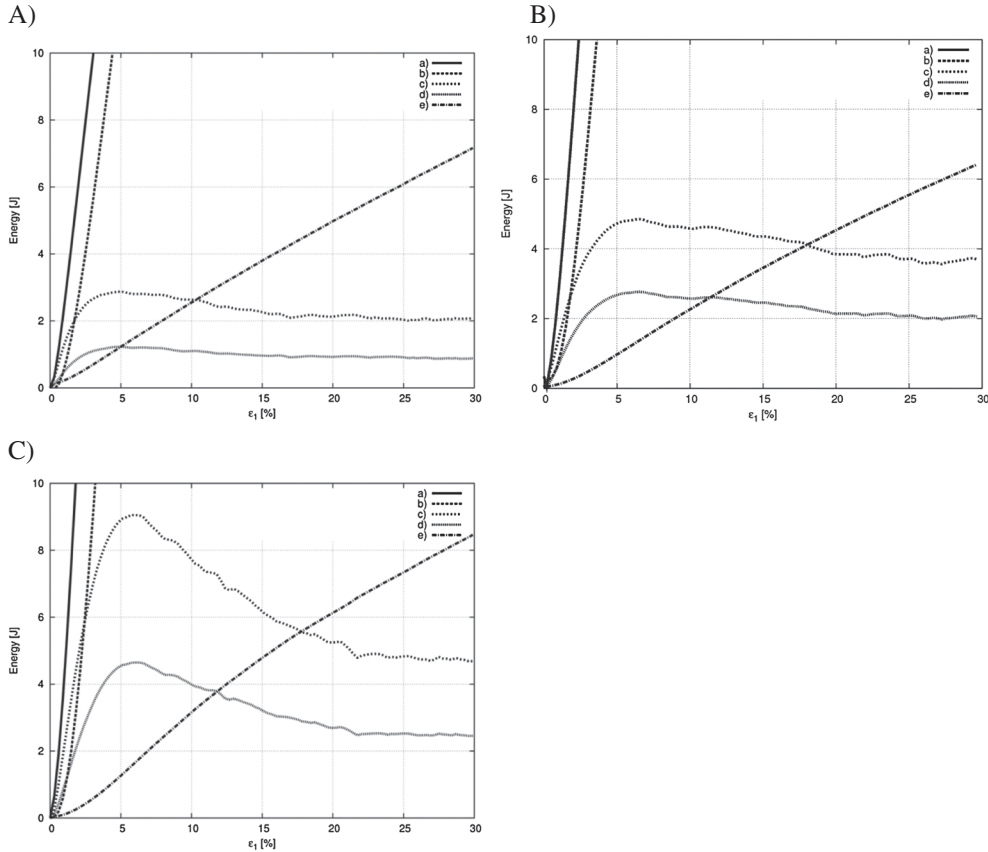
Figure 16. Calculated evolution of (a) total energy E, (b) plastic dissipation D_p, (c) elastic energy in normal direction E_c^n, (d) elastic energy in tangential direction E_c^s and (e) numerical non-viscous damping D_n ($E_c = 0.3$ GPa, $v_c = 0.3$, $\mu = 30°$) during homogeneous triaxial compression test ($e_o = 0.53$, $\sigma_c = 200$ kPa, $d_{50} = 5.0$ mm): (A) grain shape mixture 'A' of Figure 14, (B) grain shape mixture 'B' of Figure 14 and (C) grain shape mixture 'C' of Figure 14.
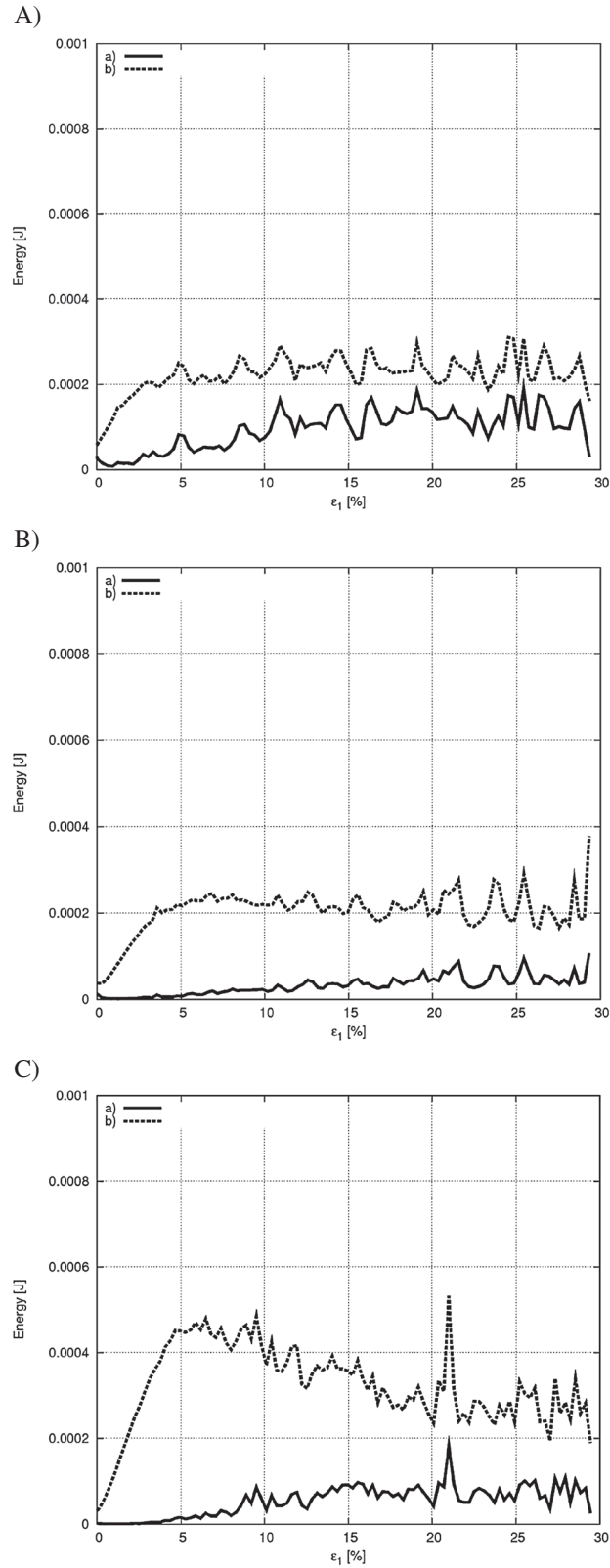
A)

B)

C)

Figure 17. Calculated evolution of kinetic energy E_c ($E_c = 0.3$ GPa, $v_c = 0.3$, $\mu = 30°$) during homogeneous triaxial compression test with rigid walls ($e_o = 0.53$, $\sigma_c = 200$ kPa, $d_{50} = 5.0$ mm): (a) rotational kinetic energy, (b) translational kinetic energy, (A) grain shape mixture 'A' of Figure 14, (B) grain shape mixture 'B' of Figure 14 and (C) grain shape mixture 'C' of Figure 14.

discrete material parameters were used as in Section 3.1. The aspect index a and the convexity indexes c_1 and c_2 are given for grain shapes 'a', 'b' and 'c' of Figure 15 and grain shape mixtures 'A', 'B' and 'C' in Table I.

The highest elastic modulus, maximum internal friction angle and dilatancy angle occur with the grain shape mixture of Figure 14C ($E=90$ MPa, $\phi_{max}=49°$, $\psi=50°$), then with the grain shape mixture, of Figure 14B ($E=70$ MPa, $\phi_{max}=42°$, $\psi=38°$) and the smallest ones with the grain shape mixture of Figure 14A ($E=55$ MPa, $\phi_{max}=28°$, $\psi=35°$) (Figure 15). They increase with increasing index c_2 [26] (because of three different mixtures only, it was impossible to define the dependence type). The critical internal friction angle for the grain shape mixtures 'B' and 'C' is the same ($\phi_{cr}=31.6°$) and smaller for the grain shape mixture 'A' ($\phi_{cr}=26°$) (Figure 15). The results with the grain shape mixture of Figure 14B are in good accordance with the experiments with respect to the stresses and volume changes (although the peak stress is still too early obtained), Figure 15. The calculated volume changes in Figure 15B are more realistic than in Figure 2B.

The energies are obviously directly connected to the specimen strength (Figure 16). The highest total energy, damping and elastic energy is with the grain shape mixture of Figure 14C, and the smallest one with the grain shape mixture of Figure 14A (Figure 16). The elastic energy and its fall rate after the peak with the grain shape mixture of Figure 14B (Figure 16B) is smaller than with the symmetric clusters composed of six spheres (Figure 9A). The highest kinetic energy is with the grain shape mixture of Figure 14C (Figure 17). The kinetic energy with the grain shape mixture of Figure 14B (Figure 17) is two to three times smaller than with the symmetric clusters composed of six spheres (Figure 12A).

3.3. Effect of grain size distribution, grain size range, mean grain size and specimen size

In order to shorten the computation time, the DEM calculations were carried out with spheres and contact moments using the following discrete material parameters: $E_c=0.3$ GPa, $v_c=0.3$, $\mu=18°$, $\beta=0.7$ and $\eta=0.4$ to match approximately experimental results for real sand by Wu [24]. The specimen size $10\times 10\times 10$ cm^3, mean grain diameter $d_{50}=5$ mm and linear grain size range 2.5–7.5 mm were mainly used. About 6,600 ($d_{50}=5$ mm, grain size range 2.5–7.5 mm) – 53,000 ($d_{50}=2.5$ mm, grain size range 1.25–3.75 mm) spheres were used. The computation time was 2–16 days using PC 3 GHz.

Initially, the effect of a stochastic distribution of spheres on the curve $\sigma_1=f(\varepsilon_1)$ was investigated at $e_o=0.53$ (Figure 18). The results from five different discrete simulations indicate a noticeable effect on
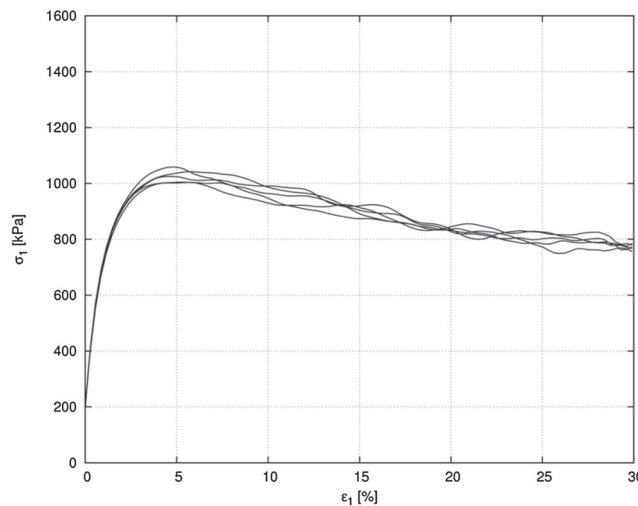

Figure 18. Effect of stochastic distribution of spheres with contact moments on vertical normal stress σ_1 versus vertical normal strain ε_1 from five different discrete simulations of homogeneous triaxial compression test with rigid walls ($E_c=0.3$ GPa, $v_c=0.3$, $\mu=18°$, $\beta=0.7$ and $\eta=0.4$) with initially dense specimen 10×10 10 cm^3 ($e_o=0.53$, $\sigma_c=200$ kPa, $d_{50}=5.0$ mm).
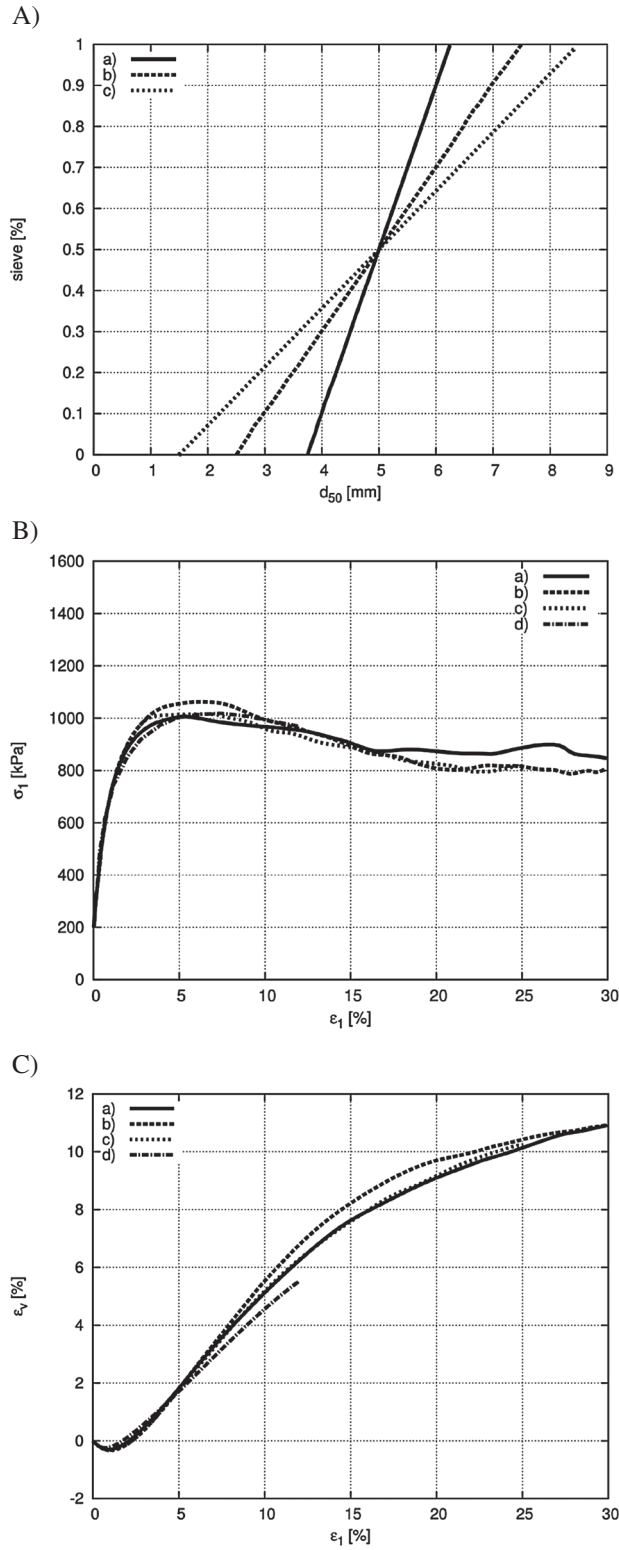
A)

B)

C)

Figure 19. Effect of grain size range (A) on vertical normal stress σ_1 versus vertical normal strain ε_1 (B) and volumetric strain ε_v versus vertical normal strain ε_1 (C) from discrete simulations with spheres and contact moments ($E_c = 0.3$ GPa, $\upsilon_c = 0.3$, $\mu = 18°$, $\beta = 0.7$ and $\eta = 0.4$, specimen size $10 \times 10 \times 10$ cm^3) during homogeneous triaxial compression test with rigid walls ($e_o = 0.53$, $\sigma_c = 200$ kPa, $d_{50} = 5.0$ mm): (a) linear grain size range 3.75–6.25 mm, (b) linear grain size range 2.5–7.5 mm, (c) linear grain size range 1.5–8.5 mm and (d) experiment.

ϕ_{max} and ε_1 corresponding to ϕ_{max}. The peak internal friction angle ϕ_{max} may differ by 2° and the vertical normal strain ε_1 corresponding to ϕ_{max} by 10%.

The effect of a grain size range (size polydispersity) on the curves $\sigma_1 = f(\varepsilon_1)$ and $\varepsilon_v = f(\varepsilon_1)$ is demonstrated in Figure 19 ($e_o = 0.53$). In contrast to DEM results with different types of the size distribution [27, 39], the effect of a linear grain size range was investigated only. The discrete results with the linear grain size range 3.75–6.25, 2.5–7.5 and 1.5–8.5 mm at $d_{50} = 5$ mm were compared. The size polydispersity effect is rather small in our calculations because of the lack of shear localization and is more affected by a stochastic distribution. The agreement of the calculated curves with the experiment is even better with spheres and contact moments (Figure 19) than with symmetric clusters (using the cluster of six spheres with material parameters from Section 3,
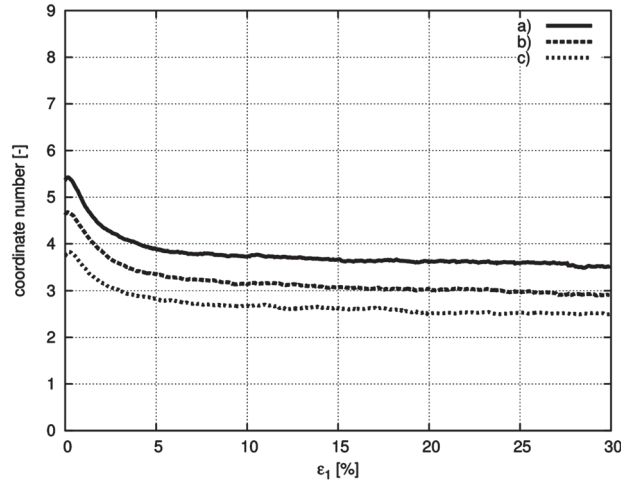

Figure 20. Evolution of coordination number from discrete simulations with spheres and contact moments ($E_c = 0.3$ GPa, $v_c = 0.3$, $\mu = 18°$, $\beta = 0.7$ and $\eta = 0.4$, specimen size $10 \times 10 \times 10$ cm^3) during homogeneous triaxial compression test with rigid walls ($e_o = 0.53$, $\sigma_c = 200$ kPa, $d_{50} = 5.0$ mm): (a) linear grain size range 3.75–6.25 mm, (b) linear grain size range 2.5–7.5 mm and (c) linear grain size range 1.5–8.5 mm.
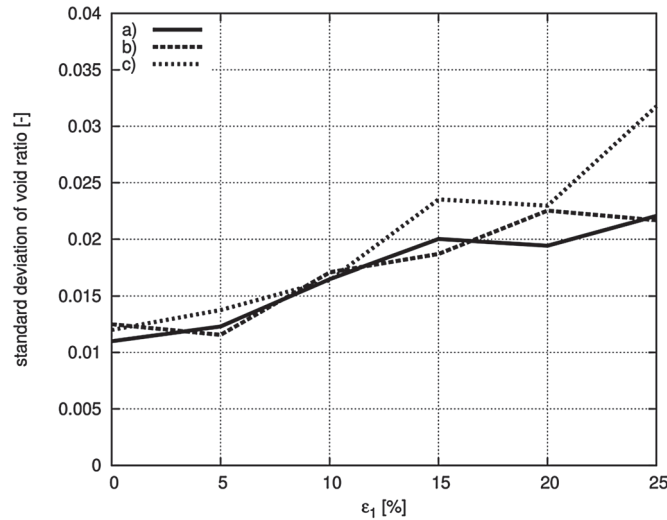

Figure 21. Evolution of standard deviation of void ratio in vertical mid-section of thickness d_{50} from discrete simulations with spheres and contact moments ($E_c = 0.3$ GPa, $v_c = 0.3$, $\mu = 18°$, $\beta = 0.7$ and $\eta = 0.4$, specimen size $10 \times 10 \times 10$ cm^3) during homogeneous triaxial compression test with rigid walls ($e_o = 0.53$, $\sigma_c = 200$ kPa, $d_{50} = 5.0$ mm): (a) linear grain size range 3.75–6.25 mm, (b) linear grain size range 2.5–7.5 mm and (c) linear grain size range 1.5–8.5 mm.

Figure 2) because symmetric sphere clusters did not correspond to the real grain shape. In addition, more calibration parameters were used to describe the model with spheres and contact moments. Because of the lack of experimental data results at the grain level, it is, however, not possible to state in general at present which discrete model is more realistic.

The highest coordination number is for the narrowest grain size range (Figure 20). The variance of a local density is similar up to $\varepsilon_1 = 10\%$ (Figure 21). Later, the standard deviation becomes the largest with the widest grain size range 1.5–8.5 mm.

The effect of the mean grain diameter d_{50} ($d_{50} = 2$–10 mm) with the specimen size $h = 10$ cm ($d_{50}/h = 0.025$–0.1) is shown in Figure 22. The larger the ratio d_{50}/h, the slightly higher the ϕ_{max} and ψ. This grain size effect is negligible because of the lack of shear localization and is rather caused by a stochastic grain distribution (Figure 18).

The results with the smaller specimen size $5 \times 5 \times 5$ cm^3 ($e_o = 0.53$, $d_{50} = 5$ mm, $d_{50}/h = 0.01$) demonstrate that the effect of the specimen size on the stress results is significant because of the
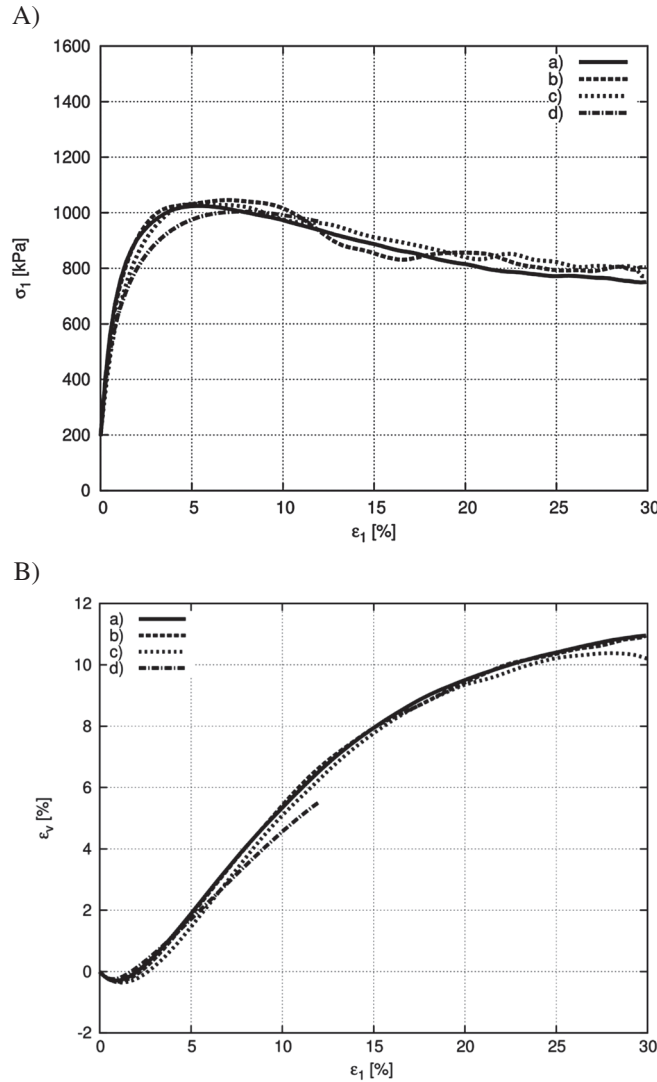
A)

B)

Figure 22. Effect of mean grain size on vertical normal stress σ_1 versus vertical normal strain ε_1 (A) and volumetric strain ε_v versus vertical normal strain ε_1 (B) from discrete simulations ($E_c = 0.3$ GPa, $v_c = 0.3$, $\mu = 18°$, $\beta = 0.7$ and $\eta = 0.4$, specimen size $10 \times 10 \times 10$ cm^3) with spheres and contact moments and rigid walls compared with experiments [23] during homogeneous triaxial compression test ($e_o = 0.53$, $\sigma_c = 200$ kPa): (a) $d_{50} = 2.5$ mm with linear grain size range 1.25–3.75 mm, (b) $d_{50} = 5$ mm with grain size range 2.5–7.5 mm, (c) $d_{50} = 10$ mm with grain size range 5–15 mm and (d) experiment.

presence of horizontal boundaries if $d_{50}/h > 0.01$ (Figure 23). The smaller the specimen, the higher the ϕ_{max} and ϕ_{cr}, and stress fluctuations. The volume changes are not influenced by the specimen size.

The calculated results of Figure 24 show that the total energy (without contact moments) increases with increasing specimen size and grain size range. The elastic energy in the tangential direction becomes higher with increasing specimen size, grain size range and mean grain size. The elastic energy in the normal direction increases with increasing specimen size. The numerical non-viscous force damping grows with increasing specimen size, grain size range and decreasing mean grain diameter.

3.4. Effect of roughness and stiffness of boundaries

The DEM calculations were again carried out with spheres and contact moments ($E_c = 0.3$ GPa, $v_c = 0.3$, $\mu = 18°$, $\beta = 0.7$ and $\eta = 0.4$). The low initial void ratio ($e_o = 0.53$), specimen size $10 \times 10 \times 10$ cm^3, mean grain diameter $d_{50} = 5$ mm and linear grain size range 2.5–7.5 mm were used.
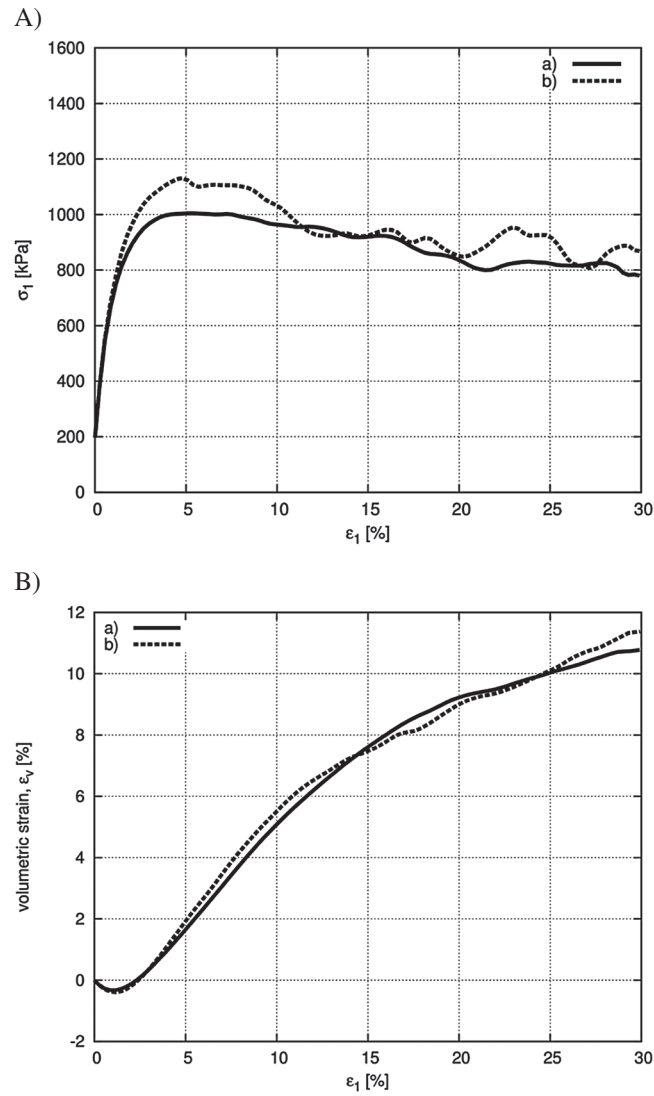

Figure 23. Effect of specimen size on vertical normal stress σ_1 versus vertical normal strain ε_1 (A) and volumetric strain ε_v versus vertical normal strain ε_1 (B) from discrete simulations with spheres and contact moments ($E_c = 0.3$ GPa, $v_c = 0.3$, $\mu = 18°$, $\beta = 0.7$ and $\eta = 0.4$) during homogeneous triaxial compression test with rigid walls ($e_o = 0.53$, $\sigma_c = 200$ kPa, $d_{50} = 5.0$ mm): (a) specimen size $10 \times 10 \times 10$ cm^3 and (b) specimen size $5 \times 5 \times 5$ cm^3.
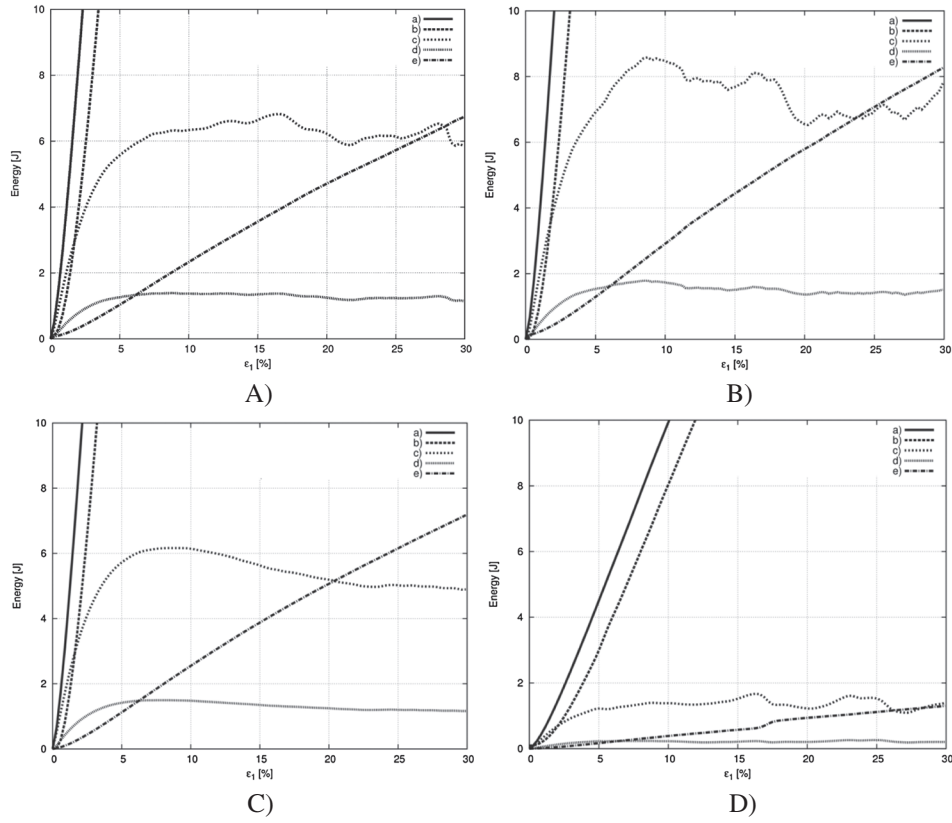
Figure 24. Calculated evolution of (a) total energy E (without contact moments), (b) plastic force dissipation D_p, (c) elastic energy in normal direction E_c^n, (d) elastic energy in tangential direction E_c^s and (e) numerical non-viscous force damping D_n from discrete simulations with spheres and contact moments ($E_c = 0.3$ GPa, $v_c = 0.3$, $\mu = 18°$, $\beta = 0.7$ and $\eta = 0.4$) during homogeneous triaxial compression test with rigid walls for (A) $10 \times 10 \times 10$ cm^3, $d_{50} = 5$ mm, grain size range 2.5–7.5 mm, (B) $10 \times 10 \times 10$ cm^3, $d_{50} = 5$ mm, grain size range 1.5–8.5 mm, (C) $10 \times 10 \times 10$ cm^3, $d_{50} = 2.5$ mm, grain size range 1.25–3.75 mm, (D) $5 \times 5 \times 5$ cm^3, $d_{50} = 5$ mm, grain size range 2.5–7.5 mm ($e_o = 0.53$, $\sigma_c = 200$ kPa, $d_{50} = 5.0$ mm).
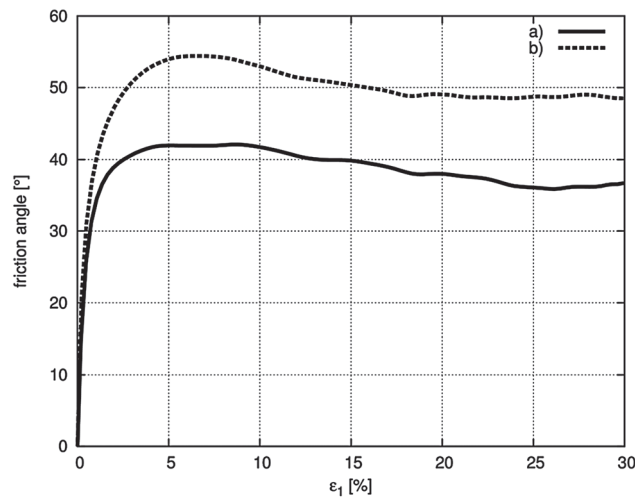

Figure 25. Effect of roughness of horizontal walls on mobilised internal friction angle versus vertical normal strain ε_1 from discrete simulations of homogeneous triaxial compression test with rigid walls for initially dense sand ($e_o = 0.53$, $\sigma_c = 200$ kPa, $d_{50} = 0.5$ mm) using spheres and contact moments ($E_c = 0.3$ GPa, $v_c = 0.3$, $\mu = 18°$, $\beta = 0.7$ and $\eta = 0.4$): (a) rough horizontal walls and (b) smooth horizontal walls.
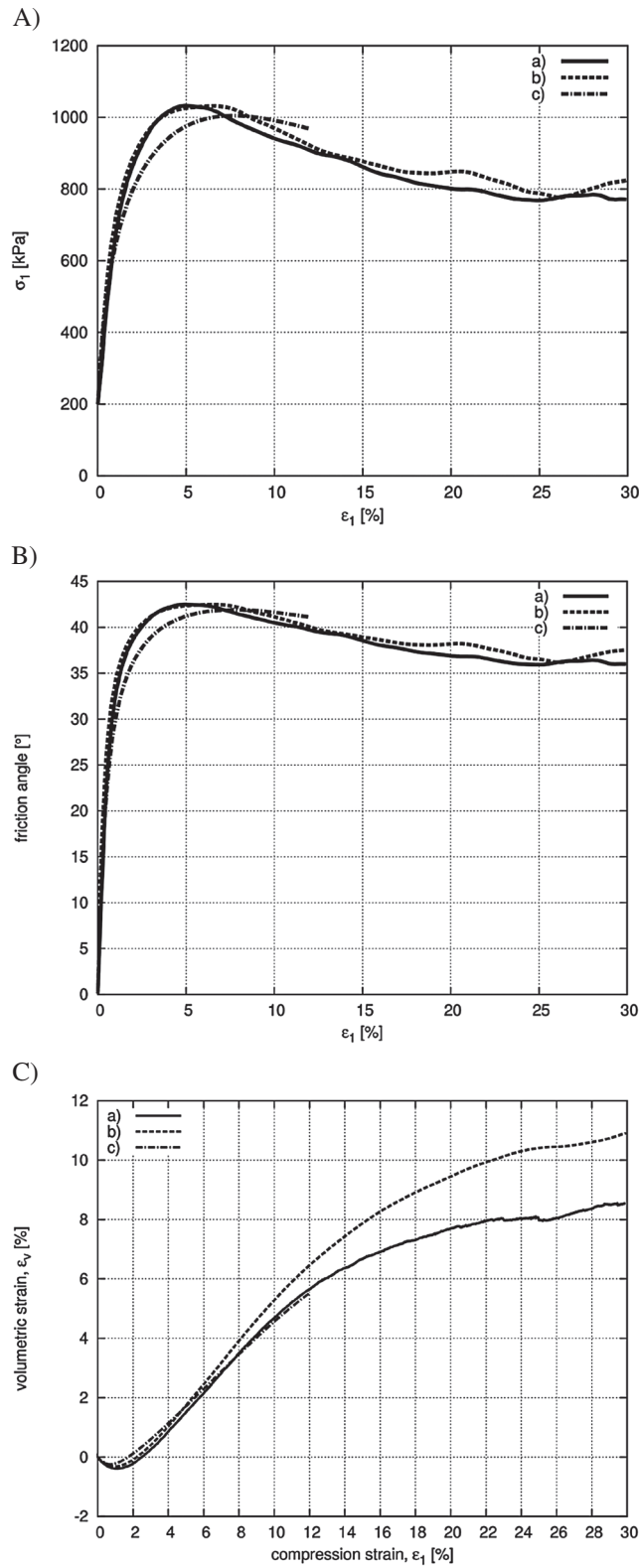
A)

B)

C)

Figure 26. Evolution of vertical normal stress σ_1 versus vertical normal strain ε_1 (A), mobilised internal friction angle versus ε_1 (B) and volumetric strain ε_v versus ε_1 (C) from discrete simulations of with spheres and contact moments and non-rigid walls ($E_c = 0.3$ GPa, $v_c = 0.3$, $\mu = 18°$, $\beta = 0.7$ and $\eta = 0.4$, specimen size $10 \times 10 \times 10$ cm^3) compared with experiments [23] during homogeneous triaxial compression test ($e_o = 0.53$, $\sigma_c = 200$ kPa, $d_{50} = 0.5$ mm): (a) membranes, (b) rigid walls and (c) experiment.

A growth of the wall friction angle between two horizontal walls and spheres from $0°$ up to $18°$ increases the peak shear resistance of the specimen from $\phi_{max}=42°$ up to $\phi_{max}=54°$, the critical internal friction angle from $\phi_{cr}=36°$ up to $\phi_{cr}=48°$ and the dilatancy angle from $\psi=34°$ up to $\psi=38°$ (Figure 25).

The effect of the stiffness of boundaries on the curves $\sigma_1=f(\varepsilon_1)$ and $\varepsilon_v=f(\varepsilon_1)$ is demonstrated in Figure 26 by using flexible membranes. When flexible membranes are taken into account, the calculation outcomes are the following: $E=70$ MPa, $\phi_{max}=42.6°$, $\phi_{cr}=36.2°$ and $\psi=33.5°$. Thus, the values of E, ϕ_{max} and ϕ_{cr} are similar as for rigid walls ($E=78$ MPa, $\phi_{max}=42.5°$, $\phi_{cr}=36.5°$). The dilatancy angle is smaller than for rigid walls ($\psi=36°$) and is closer to the measured value. The coordination number becomes lower (Figure 27) because of deformable boundaries (Figure 28). It is almost constant during deformation after the instant reduction because of the lateral pressure action (Figure 27)
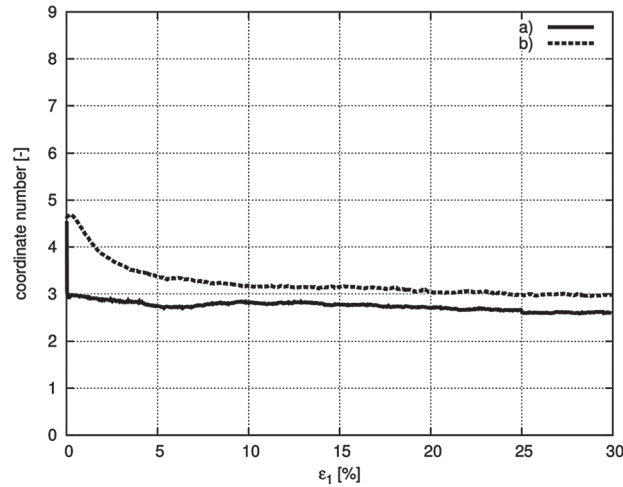

Figure 27. Evolution of coordination number from discrete simulations with spheres and contact moments ($E_c=0.3$ GPa, $v_c=0.3$, $\mu=18°$, $\beta=0.7$ and $\eta=0.4$, specimen size $10\times10\times10$ cm^3) during homogeneous triaxial compression test ($e_o=0.53$, $\sigma_c=200$ kPa, $d_{50}=5.0$ mm): (a) membranes and (b) rigid walls.

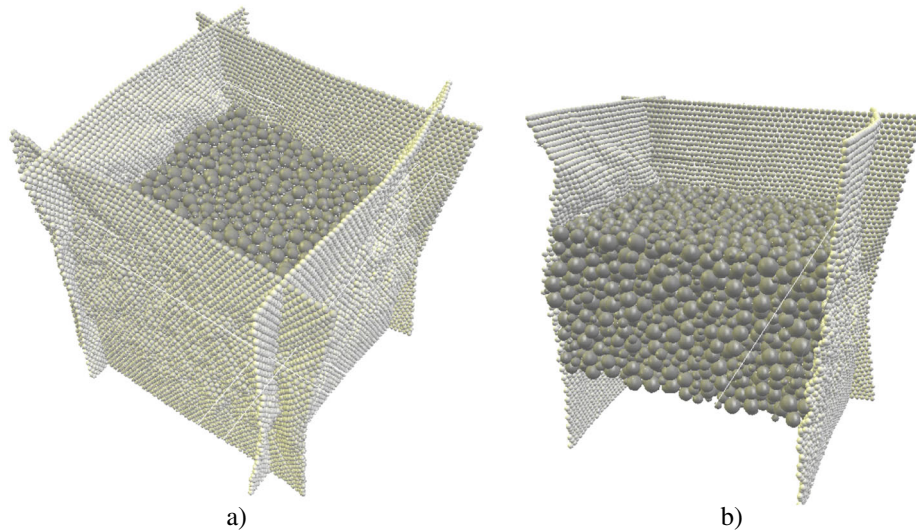a)   b)

Figure 28. Deformed initially dense specimen with flexible membranes at $\varepsilon_1=30\%$: (a) entire specimen and (b) specimen without front membrane.

4. CONCLUSIONS

The following main conclusions can also be drawn based on discrete simulations of a homogeneous drained triaxial compression test with cohesionless sand being by far the most common laboratory test used to measure the mechanical properties of granular soils:

- Both discrete models (one using clusters of spheres and the second using spheres with contact moments) are capable of closely reproducing the behaviour of cohesionless sand in the elastic, contraction and dilatancy phase and at the critical state, in spite of the fact that the real grain shape, mean grain size and grain size distribution of Karlsruhe were not taken into account. Moreover, the assembling procedure was unable to produce really initially loose specimens and provided too high coordination numbers in dense specimens. At large strains, the granular specimen reaches always a critical state independent of its initial void ratio. The results are very sensitive to the assumed approach, in particular to the grain shape. The stochastic effect is also non-negligible. It is necessary to calibrate DEM based on triaxial tests results within wide range of initial densities and confining pressures.
- The rigid walls can be assumed in discrete calibration simulations of a real triaxial homogeneous compression test with flexible membranes. The modulus of elasticity, mobilised internal friction angle and dilatancy angle practically do not depend on the rigidity of vertical boundaries.
- The grain shape irregularity causes a significant increase of the strength and volume changes. The elastic modulus, maximum internal friction angle and dilatancy angle increase with increasing convexity index c_2.
- The granulate strength increases with decreasing initial void ratio, specimen size and linear grain size distribution, and increasing mean grain diameter and roughness of horizontal boundaries. The granulate dilatancy increases with decreasing initial void ratio and specimen size and increasing mean grain diameter and roughness of horizontal boundaries.
- The peak internal friction angle increases with increasing grain convexity index c_2. The variance of a local density field is larger in initial dense sand and grows with increasing grain size range width.
- The size effect due to the mean grain diameter and specimen height is negligible when $d_{50}/h < 0.01$.
- The total energy, damping and elastic energy increase with increasing specimen size, mean grain size and initial void ratio.
- The number of contact forces is higher in initially dense sand. During deformation, it grows in initially loose sand and reduces in initially dense sand. The contact forces may be higher in initially loose sand. The void ratio distribution is more non-uniform in initially loose sand. The coordination number decreases in initially dense specimen and grows in initially loose specimen. It is smaller with grains simulated by spheres with contact moments and when using flexible vertical walls.
- The kinetic energy shows fluctuations, which correspond to the evolution of the elastic energy and damping rate. The transitional kinetic energy is higher than the rotational one. The translational and rotational kinetic energy are higher in initially dense sand and for more non-uniform grain shapes.
- Initially, the boundary external work is converted into the elastic energy. At the residual state, the almost total external boundary work is dissipated by plastic deformation. The evolution of the elastic energy in initially dense sand is related to dilatancy that reduces the normal contact forces and the number of contact points. The elastic energy decreases during the dilative deformation process and tends to a steady state corresponding to a critical state condition. In initially loose sand, it continuously decreases during a contractant and following dilatant phase.

REFERENCES

1. Tejchman J. FE modeling of shear localization in granular bodies with micro-polar hypoplasticity. In Springer Series in Geomechanics and Geoengineering, Wu W, Borja RI (eds). Springer Verlag: Berlin-Heidelberg, 2008.
2. Rojek J. Discrete element modelling of rock cutting. *Computer Methods in Materials Science* 2007; **7**(2):224–230.
3. Nitka M, Combe G, Dascalu C, Desrues J. Two-scale modeling of granular materials: a DEM-FEM approach. *Granular Matter* 2011; **13**:277–281.
4. Kuhn MR. Structured deformation in granular materials. *Mechanics of Materials* 1999; **31**:407–442.
5. Alonso-Marroquin F, Vardoulakis I, Herrmann H, Weatherley D, Mora P. Effect of rolling on dissipation infault gouges. *Physical Review E* 2006; **74**:031306.
6. Liu X, Papon A, Mühlhaus HB. Numerical study of structural evolution in shear band. *Philosophical Magazine* 2012; **92**(28–30):3501–3519.
7. Kozicki J, Niedostatkiewicz M, Tejchman J, Mühlhaus H-B. Discrete modelling results of a direct shear test for granular materials versus FE results. *Granular Matter* 2013; **15**(5):607–627.
8. Abedi S, Rechenmacher AL, Orlando AD. Vortex formation and dissolution in sheared sands. *Granular Matter* 2012; **14**:695–705.
9. Richefeu V, Combe G, Viggiani G. An experimental assessment of displacement fluctuations in a 2D granular material subjected to shear. *Geotechnique Letters* 2012; **2**:113–118.
10. Iwashita K, Oda M. Rolling resistance at contacts in simulation of shear band development by DEM. *ASCE Journal of Engineering Mechanics* 1998; **124**(3):285–292.
11. Jiang MJ, Yu HS, Harris D. A novel discrete model for granular material incorporating rolling resistance. *Computers and Geotechnics* 2005; **32**:340–357.
12. Kozicki J, Donze FV. A new open-source software developed for numerical simulations using discrete modelling methods. *Computer Methods in Applied Mechanics and Engineering* 2008; **197**:4429–4443.
13. Belheine N, Plassiard JP, Donze FV, Darve F, Seridi A. Numerical simulations of drained triaxial test using 3D discrete element modeling. *Computers and Geotechnics* 2009; **36**(1-2):320–331.
14. Mohamed A, Gutierrez M. Comprehensive study of the effects of rolling resistance on the stress-strain and strain localization behavior of granular materials. *Granular Matter* 2010; **12**(5):527–541.
15. Widuliński L, Tejchman J, Kozicki J, Leśniewska D. Discrete simulations of shear zone patterning in sand in earth pressure problems of a retaining wall. *International Journal of Solids and Structures* 2011; **48**(7-8):1191–1209.
16. Salot C, Gotteland P, Villard P. Influence of relative density on granular materials behaviour: DEM simulations of triaxial tests. *Granular Metter* 2009; **11**(4):221–236.
17. Ng TT. Particle shape effect on macro- and micro-behaviors of monodisperse ellipsoids. *International Journal for Numerical and Analytical Methods in Geomechanics* 2009; **33**:511–552.
18. Ferellec JF, McDowell GR. A method to model realistic particle shape and inertia in DEM. *Granular Matter* 2010; **12**:459–467.
19. Maeda K, Sakai H, Kondo A, Yamaguchi T, Fukuma M, Nukudani E. Stress-chain based micromechanics of sand with grain shape effect. *Granular Matter* 2010; **12**:499–505.
20. Yan Y, Ji S. Discrete element modelling of direct shear tests for a granular material. *International Journal for Numerical and Analytical Methods in Geomechanics* 2010; **34**:978–990.
21. Matsushima T, Chang CS. Quantitative evolution of the effect of irregularly shaped particles in sheared granular assemblies. *Granular Matter* 2011; **13**:269–276.
22. Azéma E, Estrada N, Radjai F. Nonlinear effects of particle shape angularity in sheared granular media. *Physical Review E* 2012; **86**(041301):1–15.
23. Šmilauer V, Chareyre B. Yade DEM Formulation, Manual, 2011.
24. Wu W. Hypoplastizität als mathematisches Modell zum mechanischen Verhalten granularer Stoffe. *Heft 129*, Institute for Soil- and Rock-Mechanics, University of Karlsruhe, 1992.
25. Widuliński L, Kozicki J, Tejchman J. Numerical simulations of triaxial test with sand using DEM. *Archives of Hydro-Engineering and Environmental Mechanics* 2009; **56**(3-4):3–26.
26. Kozicki J, Tejchman J, Mróz Z. Effect of grain roughness on strength, volume changes, elastic and dissipated energies during quasi-static homogeneous triaxial compression using DEM. *Granular Matter* 2012; **14**(4):457–468.
27. Lee SJ, Hashash YMA, Nezami EG. Simulation of triaxial compression tests with polyhedral discrete elements. *Computers and Geotechnics* 2012; **43**:92–100.
28. Sitharam TG, Dinesh SV, Shimizu N. Micromechanical modelling of monotonic drained and undrained shear behaviour of granular media using three- dimensional DEM. *International Journal for Numerical and Analytical Methods in Geomechanics* 2002; **26**:1167–1189.
29. Gong G, Zha X, Wie J. Comparison of granular material behavior under drained triaxial and plane strain conditions using 3D simulations. *Acta Mechanica Solida Sinica* 2012; **25**(2):186–196.
30. Cundall PA, Hart R. Numerical modeling of discontinua. *Engineering Computations* 1992; **9**:101–113.
31. Kolymbas D, Wu W. Recent results of triaxial tests with granular materials. *Powder Technology* 1990; **60**(2):99–119.
32. Tejchman J. FE-simulations of a direct wall shear box test. *Soils and Foundations* 2004; **44**(4):67–81.
33. Agnolin I, Roux JN. Internal states of model isotropic granular packings. I. Assembling process, geometry, and contact networks. *Physical Review E* 2007; **76**:061302.
34. Agnolin I, Roux JN. Internal states of model isotropic granular packings. II. Compression and pressure cycles. *Physical Review E* 2007; **76**:061303.

35. Agnolin I, Roux JN. Internal states of model isotropic granular packings. III. Elastic properties. *Physical Review E* 2007; **76**:061304.
36. Thornton C, Zhang L. Numerical simulations of the direct shear test. *Chemical Engineering & Technology* 2003; **26**(2):1–4.
37. Voivret C, Radjai F, Delenne JY, El Youssoufi MS. Multiscale force networks in highly polydisperse granular media. *Physical Review Letters* 2009; **102**(178001):1–4.
38. Tordesillas A, Walker DM, Qun Lin Q. Force cycles and force chains. *Physical Review E* 2010; **81**:011302.
39. Voivret C, Radjaï F, Delenne JY, El Youssoufi MS. Space-filling properties of polydisperse granular media. *Physical Review* 2007; **E76**:021301.